13104 *J. Am. Chem. Soc.* **1998,** *120,* 13104−13120

Electronic Structure of Antiferromagnetically Coupled Dinuclear Manganese ($Mn^{III}Mn^{IV}$) Complexes Studied by Magnetic Resonance Techniques

Kai-Oliver Schäfer,[†] Robert Bittl,[†] Wolfgang Zweygart,[†] Friedhelm Lendzian,[†] Gabriele Haselhorst,[‡] Thomas Weyhermüller,[‡] Karl Wieghardt,[‡] and Wolfgang Lubitz*,[†]

Contribution from the Max-Volmer-Institut für Biophysikalische Chemie und Biochemie (PC 14), Technische Universität Berlin, Strasse des 17 Juni 135, D-10623 Berlin, FRG, and Max-Planck-Institut für Strahlenchemie, Stiftstrasse 34−36, D-45470 Mülheim a.d. Ruhr, FRG

Received August 3, 1998

Abstract: The following dinuclear exchange-coupled manganese complexes are investigated: $[dtneMn^{III}Mn^{IV}(\mu\text{-}O)_2\mu\text{-}OAc](BPh_4)_2$ (dtne = 1,2-bis(1,4,7-triazacyclonon-1-yl)ethane), $[(CH_3)_4dtneMn^{III}Mn^{IV}(\mu\text{-}O)_2\mu\text{-}OAc](BPh_4)_2$ ($(CH_3)_4$dtne = 1,2-bis(4,7-dimethyl-1,4,7-triazacyclonon-1-yl)ethane), $[(CH_3)_4dtneMn^{IV}Mn^{IV}(\mu\text{-}O)_2\mu\text{-}OAc](ClO_4)_3$, $[(tacn)_2Mn^{III}Mn^{IV}(\mu\text{-}O)_2\mu\text{-}OAc](BPh_4)_2$ (tacn = 1,4,7-triazacyclononane), $[bpy_4Mn^{III}Mn^{IV}(\mu\text{-}O)_2](ClO_4)_3$ (bpy = 2,2′-bipyridyl), and $[phen_4Mn^{III}Mn^{IV}(\mu\text{-}O)_2](ClO_4)_3$ (phen = 1,10-phenanthroline). For three of these complexes, X-ray structural data obtained on single crystals are reported here. All complexes are strongly antiferromagnetically coupled, with exchange coupling constants ranging from $J = -110$ cm^{-1} (bis-μ-oxo-μ-acetato-bridged) to -150 cm^{-1} (bis-μ-oxo-bridged). EPR investigations at X- and Q-band frequencies are reported for all five mixed-valence $Mn^{III}Mn^{IV}$ complexes. **G** tensors and ^{55}Mn hyperfine coupling constants (hfc's) were obtained by simultaneous simulation of the EPR spectra at both frequency bands. By using the vector model of exchange-coupled systems, tensor axes could be related to the molecular structure of the complexes. Hyperfine coupling constants from ^{55}Mn cw-electron−nuclear double-resonance (ENDOR) spectra were in agreement with those obtained from the simulation of the EPR spectra. Ligand hyperfine couplings (^{1}H and ^{14}N) were also measured using cw-ENDOR spectroscopy. Electron spin−echo envelope modulation spectroscopy (ESEEM) spectra yielded information about small ^{14}N hyperfine and quadrupole coupling constants that could not be resolved in the ENDOR spectra. On the basis of specifically deuterated complexes and results from orientation-selection ENDOR spectra, some proton hfc's could be assigned to positions within the complexes. Using an extended point-dipole model and the coordinates provided by the X-ray structure analysis, all dipolar hfc's of the complexes were calculated. Comparison of these hfc's with experimentally obtained values led to a consistent assignment of most hf tensors to molecular positions. The electronic structures of the investigated complexes are compared with each other, and the relevance of the results for metalloenzymes containing at least a dinuclear manganese core is discussed.

1. Introduction

Manganese complexes have been found as active sites in a number of metalloenzymes.[1−3] Prominent examples are manganese catalase (MC)[1] and the oxygen-evolving complex (OEC) of oxygenic photosynthesis photosystem II (PS II).[3,4] Both enzymes are of great biological importance: MC catalyzes hydrogen peroxide disproportionation into water and oxygen, while the OEC oxidizes water to molecular oxygen. It has been shown that MC contains a dinuclear Mn complex, whereas proper function of the OEC depends on four Mn ions. Based on X-ray absorption experiments, models for the Mn complex in the MC[5,6] and the OEC[3,4,7] have been developed. In both models, μ-oxo-bridged dimanganese units play an important role.

MC and the OEC undergo several redox changes in enzymatic function in which the Mn ions change their oxidation states. MC is active in its reduced form and cycles between the $Mn^{II}Mn^{II}$ and $Mn^{III}Mn^{III}$ states. A mixed-valence form, $Mn^{II}Mn^{III}$, has also been observed. The superoxidized $Mn^{III}Mn^{IV}$ form is catalytically inactive. From all states, EPR signals have been reported (see Haddy et al.[8] and references therein).

The OEC of PS II accumulates the oxidizing equivalents necessary for water splitting. Thereby, it passes through five intermediate states, S_0 through S_4. Except for the short-lived S_4 state, EPR signals have been obtained from all other S states, at least in specific preparations.[9−16] The most prominent signal

---

* Corresponding author: phone +49-30-314-21419, fax +49-30-314-21122, E-mail lubitz@echo.chem.tu-berlin.de.

[†] Technische Universität Berlin.

[‡] Max-Planck-Institut für Strahlenchemie.

(1) Dismukes, G. C., *Chem. Rev.* **1996**, *96*, 2909.

(2) Pecoraro, V. L., Ed. *Manganese Redox Enzymes*; VCH Publishers: Weinheim, 1992.

(3) Yachandra, V. K.; Sauer, K.; Klein, M. P. *Chem. Rev.* **1996**, *96*, 2927.

(4) Yachandra, V. K.; DeRose, V. J.; Latimer, M. J.; Mukerji, I.; Sauer, K.; Klein, M. P. *Science* **1993**, *260*, 675.

(5) Waldo, G. S.; Yu, S.; Penner-Hahn, J. E. *Biochemistry* **1991**, *30*, 10486.

(6) Waldo, G. S.; Yu, S.; Penner-Hahn, J. E. *J. Am. Chem. Soc.* **1992**, *114*, 5869.

(7) Klein, M.; Sauer, K.; Yachandra, V. *Photosynth. Res.* **1993**, *38*, 265.

(8) Haddy, A.; Waldo, G. S.; Sands, R. H.; Penner-Hahn, J. E. *Inorg. Chem.* **1994**, *33*, 2677.

(9) Messinger, J.; Robblee, J. H.; Yu, W. O.; Sauer, K.; Yachandra, V. K.; Klein, M. P. *J. Am. Chem. Soc.* **1997**, *119*, 11349.

10.1021/ja9827548 CCC: $15.00

is the so-called “multiline signal” (MLS) observed in the S_2 state.[14] It was found that EPR spectra recorded from various di-μ-oxo-bridged $\mathrm{Mn^{III}Mn^{IV}}$ complexes[17,18] are similar to the S_2 MLS. Comparable EPR spectra were also found for the superoxidized state of MC.[19−21]

An EPR spectrum with basically 16 hyperfine lines is observed for the $\mathrm{Mn^{III}Mn^{IV}}$ model systems. This has been explained as resulting from an antiferromagnetically exchange-coupled (oxo-bridged) dinuclear Mn complex with localized trapped $\mathrm{Mn^{III}}$, $S = 2$, and $\mathrm{Mn^{IV}}$, $S = 3/2$, valences and a $S_{\mathrm{eff}} = 1/2$ ground state. For such a system, the spin projection model[22] predicts resulting hyperfine couplings (hfc’s): $\mathbf{A}^{\mathrm{III}} = 2\mathbf{a}^{\mathrm{III}}$ and $\mathbf{A}^{\mathrm{IV}} = -\mathbf{a}^{\mathrm{IV}}$, where $\mathbf{a}^{\mathbf{III}}$ and $\mathbf{a}^{\mathbf{IV}}$ are the intrinsic hfc’s of $\mathrm{Mn^{III}}$ and $\mathrm{Mn^{IV}}$, respectively. With the ^{55}Mn nuclear spin of $I = {}^5/_2$, the approximation $\mathbf{a}^{\mathbf{III}} = \mathbf{a}^{\mathbf{IV}}$, and isotropic $\mathbf{g}$ and hf tensors, this results in the characteristic 16-line pattern. For anisotropic tensor values, a superposition of powder patterns from the many EPR transitions is obtained, leading, in general, to more than 16 lines. For a valence-delocalized complex with equivalent Mn ions, only 11 EPR lines are obtained in the isotropic limit. In the past, several attempts have been made to simulate the EPR spectra of dinuclear mixed-valence $\mathrm{Mn^{III}Mn^{IV}}$ complexes in model systems and in the MC and OEC.[8,23−27] Such an analysis provides detailed insight into the hf structure, spin density distribution, and electronic structure of the complex.

Except for the large hf interaction with the 100% abundant ^{55}Mn nuclei, no hfc’s of the ligand nuclei can be resolved in the EPR spectra. The ligand environment is, however, essential for enzymatic function of the metalloenzymes. These interactions can be resolved by application of EPR-derived high-resolution techniques such as electron−nuclear double resonance (ENDOR) (for reviews, see refs 28−30) and electron spin−echo envelope modulation (ESEEM).[31] These techniques have recently been successfully used to study multinuclear Mn complexes[25,32−36] and gave some information on ^{14}N hf and quadrupole couplings[34,35] and ^{1}H hfc’s of specific ligands.[32,33] A complete analysis of the hf interaction in such a complex is, however, still lacking.

In this paper, we present EPR, ENDOR, and ESSEM results for a series of five complexes with different ligand spheres: $[\mathrm{dtneMn^{III}Mn^{IV}}(\mu\text{-O})_2\mu\text{-OAc}](\mathrm{BPh_4})_2$ (dtne = 1,2-bis(1,4,7-triazacyclonon-1-yl)ethane), $[(\mathrm{CH_3})_4\mathrm{dtneMn^{III}Mn^{IV}}(\mu\text{-O})_2\mu\text{-OAc}](\mathrm{BPh_4})_2$ ($(\mathrm{CH_3})_4$dtne = 1,2-bis(4,7-dimethyl-1,4,7-triazacyclonon-1-yl)ethane), $[(\mathrm{tacn})_2\mathrm{Mn^{III}Mn^{IV}}(\mu\text{-O})_2\mu\text{-OAc}]\mathrm{ClO_4}$ (tacn = 1,4,7-triazacyclononane), $[\mathrm{bpy_4Mn^{III}Mn^{IV}}(\mu\text{-O})_2]\mathrm{ClO_4}$ (bpy = 2,2′-bipyridyl), and $[\mathrm{phen_4Mn^{III}Mn^{IV}}(\mu\text{-O})_2]\mathrm{ClO_4}$ (phen = 1,10-phenanthroline) (see Figure 1). The EPR spectra were fully analyzed by simulation/fit procedures in two different frequency bands at 9 and 34 GHz, yielding the $\mathbf{G}$ and $^{55}\mathrm{Mn^{III}}$ and $^{55}\mathrm{Mn^{IV}}$ hf tensor values and tensor axes. These data were supplemented by ^{55}Mn cw-ENDOR experiments.[25] The analysis of ^{1}H ENDOR data of all complexes led to an assignment of the various ^{1}H hf tensors. These were correlated with the molecular structure by use of an extended point-dipole model for exchange-coupled model systems.[37] The combined use of ^{14}N ENDOR and ESEEM gave some information about the ^{14}N hyperfine and quadrupole couplings. It is shown that, from the observed $\mathbf{G}$ and hf tensors, a detailed picture of the underlying electronic structure of these complexes is obtained. Such model studies pave the way for a better understanding of the enzyme systems containing di- and multinuclear Mn complexes and similar metal sites.

2. Experimental Section

2.1. Preparation of Compounds and Samples. 2.1.1. Ligand Synthesis. 1,4,7-Triazacyclononane (tacn) has been prepared using the procedure described in the literature.[38,39] The binucleating ligands 1,2-bis(1,4,7-triazacyclonon-1-yl)-ethane (dtne) and 1,2-bis(4,7-dimethyl-1,4,7-triazacyclonon-1-yl)-ethane ($(\mathrm{CH_3})_4$dtne) were synthesized using a modified method described by Weisman et al.[40] The orthoamide triazatricyclo[5.2.1.0^{4,10}]decane reacts readily with 1,2-dibromoethane to give a dibromide salt which is hydrolyzed in alkaline aqueous solution. The resulting formamide is decarboxylized in concentrated sodiumhydroxide solution.

dtne. To a solution of triazatricyclo[5.2.1.0^{4,10}]decane (15 g; 108 mmol) in acetonitrile (50 mL) was added 1,2-dibromoethane (10.2 g; 54 mmol). The mixture was kept in the dark for 3 days at room temperature. The colorless crystalline material was collected by filtration and washed with dry ether. The product was dissolved in water (75 mL) and refluxed for 5 h. The cooled solution was tranfered into a 1-L

---

(10) Åhrling, K. A.; Peterson, S.; Styring, S. *Biochemistry* **1997**, *36*, 13148.

(11) Yamauchi, T.; Mino, H.; Matsukawa, T.; Kawamori, A.; Ono, T. *Biochemistry* **1997**, *36*, 7520.

(12) Campbell, K. A.; Peloquin, J. M.; Pham, D. P.; Debus, R. J.; Britt, R. D. *J. Am. Chem. Soc.* **1998**, *120*, 447.

(13) Boussac, A.; Zimmermann, J.-L.; Rutherford, A. W.; Lavergne, J. *Nature* **1990**, *347*, 303.

(14) Dismukes, G. C.; Siderer, Y. *FEBS Lett.* **1980**, *121*, 78.

(15) Dexheimer, S. L.; Gohdes, J. W.; Chan, M. K.; Hagen, K. S.; Armstrong, W. H.; Klein, M. P. *J. Am. Chem. Soc.* **1989**, *111*, 8923.

(16) Debus, R. J. *Biochim. Biophys. Acta* **1992**, *1102*, 269.

(17) Cooper, S. R.; Calvin, M. *J. Am. Chem. Soc.* **1977**, *99*, 6623.

(18) Cooper, S. R.; Dismukes, G. C.; Klein, M. P.; Calvin, M. *J. Am. Chem. Soc.* **1978**, *100*, 7248.

(19) Khangulov, S. V.; Barynin, V. V.; Voevodskaya, N. V.; Grebenko, A. I. *Biochim. Biophys. Acta* **1990**, *1020*, 305.

(20) Pessiki, P. J.; Khangulov, S. V.; Ho, D. M.; Dismukes, G. C. *J. Am. Chem. Soc.* **1994**, *116*, 891.

(21) Ivancich, A.; Barynin, V. V.; Zimmermann, J.-L. *Biochemistry* **1995**, *34*, 6628.

(22) Sands, R. H.; Dunham, W. R. *Q. Rev. Biophys.* **1975**, *7*, 443.

(23) Zheng, M.; Khangulov, S. V.; Dismukes, G. C.; Barynin, V. V. *Inorg. Chem.* **1994**, *33*, 382.

(24) Zheng, M.; Dismukes, G. C. *Inorg. Chem.* **1996**, *35*, 3307.

(25) Zweygart, W.; Bittl, R.; Wieghardt, K.; Lubitz, W. *Chem. Phys. Lett.* **1996**, *261*, 272.

(26) Blondin, G.; Girerd, J.-J. *Chem. Rev.* **1990**, *90*, 1359.

(27) Horner, O.; Charlot, M.-F.; Boussac, A.; Anxolabéhère-Mallart, E.; Tchertanov, L.; Guilheim, J.; Girerd, J.-J. *Eur. J. Inorg. Chem.* **1998**, 721−727.

(28) Hoffmann, B.; DeRose, V. J.; Doan, P. E.; Gurbiel, R. J.; Houseman, A. L. P.; Telser, J. In *Biological Magnetic Resonance, EMR of Paramagnetic Molecules*; Berliner, L. J., Reuben, J., Eds.; Plenum Press: New York, 1993; Vol. 13, p 151.

(29) Hüttermann, J. In *Biological Magnetic Resonance, EMR of Paramagnetic Molecules*; Berliner, L. J., Reuben, J., Eds.; Plenum Press: New York, 1993; Vol. 13, p 219.

(30) Kurreck, H.; Kirste, B.; Lubitz, W. *Electron Nuclear Double Resonance Spectroscopy of Radicals in Solution*; VCH: Weinheim, 1988.

(31) Dikanov, S. A.; Tsvetkov, Y. D. *Electron Spin Echo Envelope Modulation (ESEEM) Spectroscopy*; CRC Press: Boca Raton, FL, 1992.

(32) Tan, X. L.; Gultneh, Y.; Sarneski, J. E.; Scholes, C. P. *J. Am. Chem. Soc.* **1991**, *113*, 7853.

(33) Khangulov, S.; Sivaraja, M.; Barynin, V. V.; Dismukes, G. C. *Biochemistry* **1993**, *32*, 4912.

(34) Tang, X.-S.; Sivaraja, M.; Dismukes, G. C. *J. Am. Chem. Soc.* **1993**, *115*, 2382.

(35) Randall, D. W.; Sturgeon, B. E.; Ball, J. A.; Lorigan, G. A.; Chan, M. K.; Klein, M. P.; Armstrong, W. H.; Britt, R. D. *J. Am. Chem. Soc.* **1995**, *117*, 11780.

(36) Randall, D.; Gelasco, A.; Caudle, M.; Pecoraro, V.; Britt, R. *J. Am. Chem. Soc.* **1997**, *119*, 4481.

(37) (a) Zweygart, W. ESR- und ENDOR-Untersuchungen an mehrkernigen gemischtvalenten Mangankomplexen als Modelle für das wasseroxidierende Enzymsystem im Photosystem II. Doctoral thesis, Technische Universität, Berlin, 1995. (b) Fiege, R.; Zweygart, W.; Bittl, R.; Adir, N.; Renger, G.; Lubitz, W. *Photosynth. Res.* **1996**, *48*, 227.

(38) Atkins, J. E. R.; Oettle, W. F. *Org. Synth.* **1978**, *58*, 86.

(39) Wieghardt, W.; Schmidt, B. N.; Weiss, J. *Chem. Ber.* **1979**, *112*, 2220.

(40) Weisman, G. R.; Vachon, D. J.; Johnson, V. B.; Gronbeck, D. A. *J. Chem. Soc., Chem. Commun.* **1987**, 886.

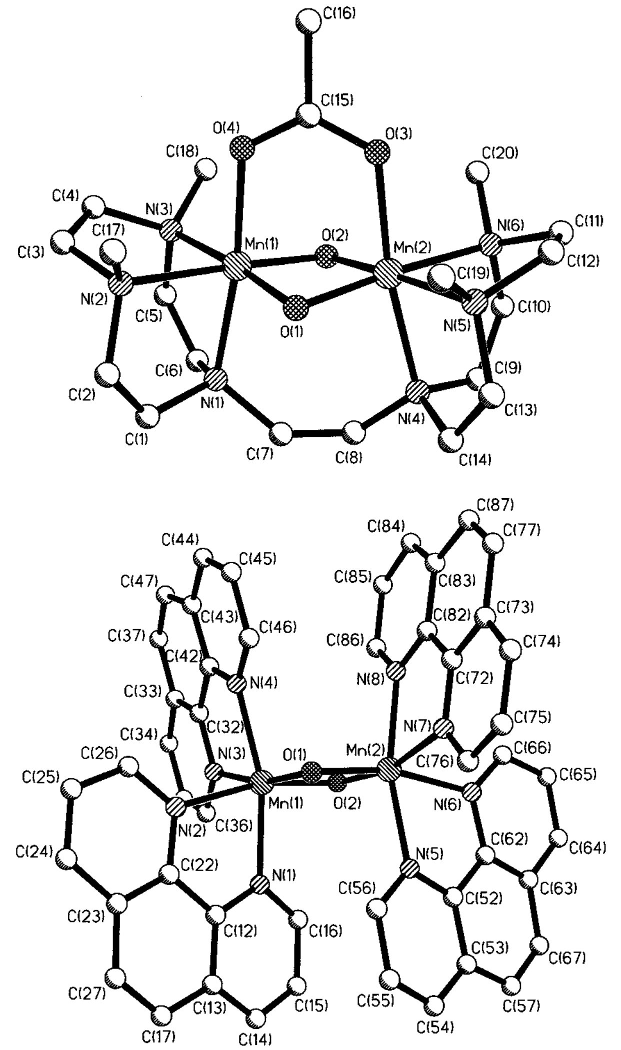

Figure 1. Schematic representation of the crystal structures of complexes **2** (top) and **6** (bottom). Coordinates of **6** were taken from ref 63. In complex **1**, the four methyl groups C17, C18, C19, and C20 present in **2** are replaced by protons. Complex **4** additionally lacks the ethylidene bridge (C7 and C8); instead, there are protons attached to N1 and N4. Complexes **5** and **6** differ in the following way: the carbon atoms C17, C27, C37, C47, C57, C67, C77, and C87 in **6** are replaced by hydrogens in **5**. Hydrogen atoms are not shown.

three-necked flask equipped with an efficient stirrer and a water separator. Sodium hydroxide (15 g) was carefuly dissolved in portions and toluene (300 mL) added. The water was removed by azeotropic distillation under vigorous stirring. When all water had been separated, more NaOH (10 g) was added. From the filtered solution, toluene was removed under vacuum. The colorless oil solidified within a few days. Yield: 12 g (78%).

$(CH_3)_4$dtne. In 23 g of formic acid, powdered dtne (10 g; 35 mmol) was dissolved successively while cooling in an ice bath. An aqueous formaldehyde solution (15 mL (37%); 188 mmol) was added, and the mixture was refluxed for 10 h. To the cooled mixture was added 40 mL of concentrated HCl. After removal of the solvent by rotary evaporation, the methylated ligand was isolated as its hydrochloride. The hydrochloride was dissolved in water (40 mL) and NaOH added (15 g). The solution was extracted several times with ether, and the combined organic fractions were dried with anhydrous Mg_2SO_4. Removal of the solvent under reduced pressure yielded 10.5 g (88%) of $(CH_3)_4$dtne. 400 MHz ^{1}H NMR (CD_3CN): δ 2.31 (s, 12H), 2.6 (m, 28H).

2.1.2. Preparation of the Deuterated Ligands. Deuterated ligands were synthesized as described above, but deuterated dibromethane-d_4, formic acid-d_2, and formaldehyde-d/D_2O were used for the preparations according to published procedures.

Deuterated reagents were obtained from commercial sources (dibromethane-d_4, formaldehyde-d_2, formic acid-d, D_2O, and sodium acetate-d_3 (d > 98%)). Completeness of C-deuteration of the ligands was checked by ^{1}H NMR spectroscopy.

Metal complexes with N-deuterated ligands (H−D exchange of acidic protons in MeCN/D_2O) and acetate-d_3 (acetate exchange) were examined by IR and ESI mass spectroscopy. Impurities ≤5% cannot be excluded by these methods.

2.1.3. Preparation of Complexes. [dtne$Mn^{III}Mn^{IV}$(μ-O)$_2$(μ-OAc)]$(BPh_4)_2$ (1). To a stirred solution of dtne (0.5 g; 1.75 mmol) in methanol (40 mL) was added $[(OH_2)_3Mn^{III}_3(\mu_3\text{-}O)(\mu\text{-}OAc)_6]$OAc (Mn(III) acetate) (1 g; 1.5 mmol). The resulting green solution was mixed with sodium tetraphenylborate (1 g; 2.9 mmol) in 20 mL of methanol. The green precipitate was collected by filtration and recrystallized from acetonitrile. Single crystals for X-ray diffraction were obtained from a hot saturated solution in acetonitrile which was allowed to cool slowly overnight. Yield: 1.02 g (52%). Anal. Calcd for $C_{64}H_{75}B_2Mn_2N_6O_4$: C, 68.40; H, 6.73; N, 7.48. Found: C, 67.4; H, 6.8; N, 7.3. UV/vis (CH_3CN) λ_{max}/nm (ϵ/L mol^{-1} cm^{-1}): 375 (sh), 445 (sh), 555 (280), 636 (270).

$[(CH_3)_4$dtne$Mn^{III}Mn^{IV}(\mu$-O)$_2(\mu$-OAc)](ClO_4) (2a). To a solution of $(CH_3)_4$dtne (0.5 g; 1.5 mmol) in methanol (40 mL) was added Mn(III) acetate (l g; 1.5 mmol). The red solution was allowed to stand for 3 days exposed to air after addition of anhydrous $NaClO_4$ (3 g; 25 mmol). The almost black precipitate was filtered off and recrystallized from hot water, giving dark green needles. Yield: 0.6 g (64%). Anal. Calcd for $C_{20}H_{43}Cl_2Mn_2NO_{12}$: C, 32.45; H, 5.85, N, 11.35. Found: C, 32.8; H, 5.8; N, 11.2. UV/vis (CH_3CN) λ_{max}/nm (ϵ/L mol^{-1} cm^{-1}): 273 (15 400), 385 (sh), 430 (sh), 552 (360), 638 (380), 800 (sh). Single crystals suitable for X-ray diffraction were obtained from the tetraphenylborate salt.

$[(CH_3)_4$dtne$Mn^{III}Mn^{IV}(\mu$-O)$_2(\mu$-OAc)]$(BPh_4)_2$ (2). A solution of **2a** (0.3 g; 0.4 mmol) in acetonitrile (25 mL) was mixed with a solution of $NaBPh_4$ (0.28 g; 0.8 mmol) in acetonitrile (10 mL). Slow evaporation of the solvent yielded green crystals (0.3 g; 64%). Anal. Calcd for $C_{68}H_{83}B_2Mn_2N_6O_4$: C, 69.22; H, 7.09; N, 7.12. Found: C, 69.4; H, 6.9; N, 7.0.

$[(CH_3)_4$dtne$Mn^{IV}_2(\mu$-O)$_2(\mu$-OAc)]$(ClO_4)_3$ (3). To a green solution of **2a** (0.5 g; 0.6 mmol) in water (25 mL) was added perchloric acid (0.5 mL; 70% aq). Dark brown microcrystals precipitated almost instantly which were recrystallized from hot water. Single crystals were grown by cooling the hot solution slowly overnight. Yield: 0.32 g (63%). Anal. Calcd for $C_{20}H_{43}Cl_3Mn_2N_6O_{16}$: C, 28.60; H, 5.16; N, 10.01. Found: C, 29.0; H, 5.3; N, 10.1. UV/vis (CH_3CN) λ_{max}/nm (ϵ/L mol^{-1} cm^{-1}): 310 (16 000), 465 (2200), 588 (520), 640 (sh).

[(tacn)$_2Mn^{III}Mn^{IV}(\mu$-O)$_2(\mu$-OAc)]$(BPh_4)_2$ (4). The complex was prepared as described in the literature.[41]

[(bpy)$_4Mn^{III}Mn^{IV}(\mu$-O)$_2$]$(ClO_4)_3$ (5) and **[(phen)$_4Mn^{III}Mn^{IV}(\mu$-O)$_2$]$(ClO_4)_3$ (6)** have been prepared following published procedures.[17]

2.1.4. Preparation of Deuterated Complexes. The C-deuterated complexes were prepared from the corrosponding ligands. The N-deuterated compounds were obtained by NH/ND exchange. The dtne and tacn complexes were dissolved in acetonitrile/D_2O mixtures (10:1). The solutions were allowed to stand for 5 h at ambient temperature, followed by pumping off the solvent. The acetato-d_3 complexes were prepared by OAc−/OAc-d_3− exchange. **(C)-1-d_4** has been prepared from the corresponding labeled ligand.

2.2. X-ray Crystallographic Data Collection and Refinement of the Structures. Green single crystals of **1** and **2** and a brown crystal of **3** were mounted in sealed glass capillaries. Graphite-monochromated Mo Kα radiation (λ = 0.710 73 Å) was used throughout. Crystallographic data of the compounds and diffractometer types used are given in Table 1. Data were corrected for Lorentz and polarization effects. A semiempirical absorption correction (ψ-scan) was applied for **1** and **3**. The program SADABS[42] was used for absorption correction of **2**. The

---

(41) Wieghardt, K.; Bossek, U.; Zsolnai, L.; Huttner, G.; Blondin, G.; Girerd, J.-J.; Babonneau, F. *J. Chem. Soc., Chem. Commun.* **1987**, 651.

(42) Sheldrick, G. M. *SADABS*; Universität Göttingen, 1994.

Table 1. Crystallographic Data for Complexes **1**, **2**, and **3**

	1	**2**	**3**
chem formula	$C_{64}H_{75}B_2Mn_2N_6O_4$	$C_{68}H_{83}B_2Mn_2N_6O_4$	$C_{20}H_{43}Cl_3Mn_2N_6O_{16}$
fw[a]	1123.8	1179.9	839.8
space group	$P\bar{1}$	$P\bar{1}$	*Imm*2
a, Å	10.996(4)	13.040(2)	9.025(1)
b, Å	14.329(6)	13.125(2)	12.435(2)
c, Å	18.021(8)	19.951(3)	14.944(2)
α, deg	85.39(3)	97.22(2)	90
β, deg	80.54(3)	100.08(2)	90
γ, deg	88.01(3)	113.86(2)	90
V, $Å^3$	2791(2)	3000.5(8)	1677.1(8)
Z	2	2	2
T, K	293(2)	100(2)	293(2)
ρ_{calcd}, g cm^{-3}	1.337	1.306	1.663
diffractometer used	Siemens P4	Siemens SMART	Nicolet R3m/V
no. of data	8973	11 021	1111
unique obsd data[b]	5585	5062	876
no. of params	719	739	85
μ (Mo Kα), cm^{-1}	5.08	4.76	10.4
R[c]	0.053	0.071	0.098
R_w[d] (all data)	0.143	0.179	

[a] fw = formula weight. [b] Observation criterion: $I > 2\sigma(I)$. [c] $R = \sum||F_o| - |F_c||/\sum|F_o|$. [d] $R_w = (\sum w(F_o^2 - F_c^2)^2/\sum w(F_o^2)^2)^{1/2}$, where $w = 1/\sigma^2(F_o^2) + (aP)^2 + bP$, $P = (F_o^2 + 2F_c^2)/3$.

Siemens SHELXTL[43] software package was used for solution, refinement, and artwork of the structures. All structures were solved and refined by direct methods and difference Fourier techniques. Neutral atom scattering factors were obtained from tables.[44] All non-hydrogen atoms in **1** and **2** were refined anisotropically, and all hydrogen atoms were placed at calculated positions and refined as riding atoms with isotropic displacement parameters. Complex **3** was found to be disordered on two bisecting crystallographic mirror planes, standing perpendicular to each other. Manganese, oxygen, and nitrogen atoms were refined anisotropically, whereas carbon atoms were refined isotropically. A split-atom model for the disordered carbon atoms failed due to the low resolution of data. Some oxygen atoms of the perchlorate anions could not be determined reliably due to disorder.

2.3. Magnetic Measurements. The magnetic susceptibilities of solid sample complexes were measured in the temperature range 2−300 K by using a SQUID susceptometer (MPMS Quantum Design) with an external magnetic field of 1.0 T. The data were corrected for underlying diamagnetism by use of Pascal's tabulated constants.

2.4. EPR Samples. Samples were prepared by dissolving the complex to a concentration of 10^{-3} mol/L in either highly purified dimethylformamide (DMF) (complexes **1**, **2**, and **4**) or acetonitrile (MeCN) (complexes **5** and **6**) under exclusion of oxygen and water using a high-vacuum line. All samples were sealed in quartz tubes and rapidly frozen in liquid nitrogen. Great care was taken to avoid any Mn^{II} impurities in the samples. The X-band experiments were performed at liquid helium temperature (4 K); for Q-band, a higher temperature (50 K) was selected.

2.5. EPR, ENDOR, and ESEEM. X-band (9 GHz) measurements were performed on a Bruker ESP 300E spectrometer equipped with an Oxford ESR 910 cryostat (temperature range 1.8−300 K). For the cw-ENDOR experiments on the ^1H and ^{14}N nuclei, a home-built resonator described in ref 45 was used, equipped with a 16-turn ENDOR coil, a rf signal generator (Rhode & Schwarz SMT 02), and a 200-W rf power amplifier (ENI A3200 L, 0.25−150 MHz). ^{55}Mn cw-ENDOR experiments were performed with a modified four-turn ENDOR coil and a 100-W rf power amplifier (ENI 4100 L, 1.5−400 MHz).[25] A Bruker ESP 380E spectrometer in combination with an Oxford CF 935 cryostat was used to obtain X-band ESEEM spectra.[46] Q-band (34 GHz) EPR experiments were performed on either a Bruker ER 200D or a Bruker ESP 300E spectrometer equipped with a Bruker Q-band bridge (ER 051QG), a Bruker Q-band cavity (ER 5106QT), and an Oxford CF 935 cryostat. The ER 200D spectrometer was controlled by an Atari TT/030 computer. The microwave frequency was monitored by a frequency counter (HP 5352B), and the magnetic field was measured by a Bruker NMR gaussmeter (ER 035).

2.6. Analysis of EPR Spectra. The EPR spin Hamilton operator for an exchange-coupled system consisting of two electron spins is used in the form which contains only contributions from the exchange interaction $-2JS_1S_2$, the electronic Zeemann term $\beta_e S_i \mathbf{g_i} \mathbf{B}$, the hyperfine interaction between the electron spins with the (manganese) nuclear spins $S_i \mathbf{a}_i I_i$, and the zero-field interactions $S_i \mathbf{d}_i S_i$ (i = 1, 2).

$$\mathbf{H} = -2JS_1S_2 + \beta_e(S_1\mathbf{g_1} + S_2\mathbf{g_2})\mathbf{B} + S_1\mathbf{a_1}I_1 + S_2\mathbf{a_2}I_2 + S_1\mathbf{d_1}S_1 + S_2\mathbf{d_2}S_2 \quad (1)$$

with J being the isotropic exchange coupling constant, $\mathbf{d}_i$ the zero-field splitting (zfs) tensors, β_e the Bohr magneton, **B** the magnetic field vector, $\mathbf{g}_i$ the **g** tensors, and $\mathbf{a}_i$ the hyperfine coupling tensors, respectively. S_i and I_i denote the electron spin and nuclear spin operators of the first and the second ion. The two isolated spin systems are added using the vector projection model for exchange-coupled systems.[22,26,47,48] The EPR spin Hamiltonian H_1 for the $S = {}^1/_2$ ground state is then

$$\mathbf{H_1} = \beta_e S\mathbf{G}B + S\mathbf{A_1}I_1 + S\mathbf{A_2}I_2 \quad (2)$$

The **G** tensor in the coupled representation is related to the **g** tensors of the two isolated systems $\mathbf{g_1}$ and $\mathbf{g_2}$ by (see also Zheng et al.[23])

$$\mathbf{G} = c_1\mathbf{g_1} + c_2\mathbf{g_2} + \frac{c_1c_2}{5J}(\mathbf{g_1} - \mathbf{g_2})((3c_1 + 1)\mathbf{d_1} - (3c_2 + 1)\mathbf{d_2}) \quad (3)$$

$$c_1 = \frac{S(S+1) + S_1(S_1+1) - S_2(S_2+1)}{2S(S+1)} \quad (4)$$

$$c_2 = \frac{S(S+1) - S_1(S_1+1) + S_2(S_2+1)}{2S(S+1)} \quad (5)$$

where c_1 and c_2 are the spin projection factors for coupled $Mn^{III}Mn^{IV}$ systems ($S^{III} = 2$, $S^{IV} = {}^3/_2$), $c^{III} = 2$, and $c^{IV} = -1$. The third term in eq 3 is usually neglegted in $Mn^{III}Mn^{IV}$ complexes, since the exchange

---

(43) Siemens Analytical X-ray Instruments. SHELXTL V. 5; 1994.

(44) *International Tables for X-ray Crystallography*; Kynoch Press: Birmingham, UK, 1991.

(45) Zweygart, W.; Thanner, R.; Lubitz, W. *J. Magn. Reson.* **1994**, *109*, 172.

(46) Käss, H.; Fromme, R.; Lubitz, W. *Chem. Phys. Lett.* **1996**, *257*, 197.

(47) Bencini, A.; Gatteschi, D. *EPR of Exchange Coupled Systems*; Springer-Verlag: Berlin, 1990.

(48) Bertrand, P.; Guigliarelli, B.; More, C. *New J. Chem.* **1991**, *15*, 445.

coupling J is much larger than the zero-field splitting.[49] The manganese hyperfine coupling tensors of the combined system ($\mathbf{A_1}$ and $\mathbf{A_2}$) can be expressed in a similar way. If $\mathbf{a_1}$ and $\mathbf{a_2}$ are the intrinsic hyperfine coupling tensors of the isolated ions,[23]

$$\mathbf{A_1} = c_1\mathbf{a_1} - \frac{\mathbf{a_1}}{5J}c_1c_2((3c_1 + 1)\mathbf{d_1} - (3c_2 + 1)\mathbf{d_2}) \qquad (6)$$

$$\mathbf{A_2} = c_2\mathbf{a_2} + \frac{\mathbf{a_2}}{5J}c_1c_2((3c_1 + 1)\mathbf{d_1} - (3c_2 + 1)\mathbf{d_2}) \qquad (7)$$

The zfs has a stronger influence on the Mn hfc than on the **g** tensor. In eq 3, it acts on the difference of the intrinsic **g** tensors, whereas in eqs 6 and 7, it is actually added to the hyperfine coupling. Furthermore, it can be seen from these equations that hyperfine anisotropy can be transferred from one nucleus to the other by the zfs tensors $\mathbf{d_1}$ and $\mathbf{d_2}$. This means that, even if an intrinsic hfc is isotropic, the respective coupled hfc may become anisotropic.

2.7. Simulation of EPR Spectra. The EPR simulation program used[50] calculates resonances by means of perturbation theory. The hyperfine coupling is treated as perturbation to second order of the Zeeman term of the spin Hamiltonian.[51] As Haddy et al. have shown,[8] solving the Hamiltonian to third order is not necessary for X- or Q-band frequencies; it is, however, essential for lower frequencies, such as S-band. For the simulation of the $\mathrm{Mn^{III}Mn^{IV}}$ spectra, two hyperfine tensors and one **G** tensor with their respective relative orientations expressed by the three Euler angles (α, β, and γ)[52] were used. The resonances can be folded with Lorentzian and Gaussian line shapes. To find the best set of simulation parameters, a nonlinear least-squares fitting routine[53] was incorporated.

We started fitting with isotropic **G** and hf tensors. First only g factors were adjusted to improve the fit at Q-band; at X-band, hf parameters were modified exclusively to yield a satisfactory fit. The new g and hf parameters were then incorporated in the next fitting step at X- and Q-band, respectively. Fitting was complete when a consistent set of parameters for both frequency bands was found that could not be improved any further. The difference between the simulated and experimental spectra was calculated according to ref 23.

2.8. Analysis of ENDOR Spectra. In addition to the Hamiltonian given in eq 2, we have to account for the nuclear Zeeman interaction and the hyperfine interaction between the effective electron spin and the ligand nuclear spins $\sum_{\mathrm{j}} S\mathbf{a_{\mathit{j}}}I_j$, as well as for quadrupole interactions $\sum_j I_j\mathbf{P_{\mathit{j}}}I_j$, where the summations are done over all magnetic nuclei. The resulting ENDOR spin Hamiltonian is then

$$\mathbf{H_2} = \mathbf{H_1} + \beta_{\mathrm{n}}B\sum_j g_{\mathrm{n}_j}I_j + \sum_j S\mathbf{a_{\mathit{j}}}I_j + \sum_j I_j\mathbf{P_{\mathit{j}}}I_j \qquad (8)$$

According to the first-order ENDOR resonance condition for protons,[30]

$$\nu^{\pm}_{\mathrm{ENDOR}} = |\nu_{^1\mathrm{H}} \pm \frac{A}{2}| \qquad (9)$$

line pairs occur around the proton Larmor frequency

$$\nu_{^1\mathrm{H}} = \frac{g_{\mathrm{H}}\beta_{\mathrm{n}}B}{h} \qquad (10)$$

separated by the hyperfine coupling constant A. In eq 10, g_{H} is the proton g factor and β_{n} is the nuclear magneton. Different field settings in the EPR spectrum lead to a shift of $\nu_{^1\mathrm{H}}$ which is proportional to the magnetic moment of the proton. The shift is much smaller for nuclei like ^{14}N with smaller magnetic moments. This effect was used here as an additional tool to assign the observed ENDOR lines to ^{1}H and ^{14}N, respectively (see Figure 7). For nuclei with small magnetic moments, such as ^{14}N or ^{55}Mn, ν_n is usually smaller than $A/2$ at X-band. When the magnetic field is applied along a principal axis i, the first-order ENDOR frequencies are ($I = 1$ for ^{14}N and $I = {}^5/_2$ for ^{55}Mn)[54,55]

$$\nu_{\mathrm{ENDOR}}(^{14}\mathrm{N}) = |\frac{A}{2} \pm \nu_{^{14}\mathrm{N}} \pm \frac{3P_i}{2}| \qquad (11)$$

$$\nu_{\mathrm{ENDOR}}(^{55}\mathrm{Mn}) = |\frac{A}{2} \pm \nu_{^{55}\mathrm{Mn}} \pm \frac{3P_i}{2}(2m_I^u - 1)| \qquad (12)$$

^{14}N lines appear centered around $A/2$, separated by $2\nu_{^{14}\mathrm{N}}$; they are additionally split by the electric quadrupole term, in which P_i is the principal value of the quadrupole tensor P along the axis i. m_I^u in eq 12 is the magnetic nuclear spin quantum number of the upper state of a transition with $\Delta m_I = \pm 1$. It takes $2I$ values in the range of $1 - I \leq m_I^u \leq I$. For a nonselective setting in the EPR spectrum, one could observe up to $4I$ lines in the ENDOR spectrum. For all other cases, the number of lines is smaller than $4I$.[35] The quadrupole tensor P is traceless and has the principal values P_x, P_y, and P_z; it is commonly described by $P_{\|}$ and η, with $P_{\|} = {}^3/_2 P_z = 3K/(I(2I - 1))$, with $K = e^2qQ/4h$ and the asymmetry parameter $\eta = |(P_x - P_y)/P_z|$.

2.9. Orientation-Selection ENDOR. Information about magnitude and orientation of the magnetic interactions can best be obtained by performing experiments on single crystals. However, for the complexes studied in this paper, spin−spin interactions between different sites in the single crystals result in severe broadening of the EPR lines. Diamagnetically diluted single crystals are not available, which would diminish the spin−spin interactions. Some limited information can, however, be obtained from frozen solutions by using orientation-selection ENDOR spectroscopy.[28,29,56] In this technique, subsets of molecules with specific orientation relative to the magnetic field are selected by setting the external field to specific points at the EPR powder pattern that are determined by sufficiently large **g** or hf anisotropy. This method is used here to gain information about the assignment of lines in our spectra to the components of a specific hf tensor. For orientation selection, it is necessary to know which tensor components contribute to a specific EPR line. Therefore, an exact analysis of the EPR spectra is a prerequisite for an orientation-selection ENDOR experiment.

2.10. Analysis of ESEEM Spectra. ^{14}N ENDOR spectra often suffer from superposition of hyperfine and quadrupole lines in a narrow range at low rf frequencies, in particular when the ^{14}N hfc's are small. A pulsed variant of EPR, electron spin echo envelope modulation (ESEEM) spectroscopy,[31] yields information about hf couplings and nuclear quadrupole splittings which cannot be resolved by ENDOR. For small hyperfine coupling constants, field/frequency can be varied to fulfill the "cancellation" condition $|\nu_n - |A|/2| < 2K/3$.[57] If this condition is met, the applied magnetic field and the hyperfine field almost cancel each other in one m_s state. Then, to a good approximation, the zero-field quadrupole transitions are observed at ν_+, ν_-, and ν_0 in the ESEEM spectrum. For the other m_s state, a "double-quantum" transition is obtained.[31]

The ^{14}N ESEEM spectra were evaluated using the following equations:[31,58,59]

---

(49) For example, for complex **6**, $|J| > 110$ cm^{-1}, while $D^{\mathrm{III}} = -3.4$ cm^{-1} and $E^{\mathrm{III}} = 0.116$ cm^{-1} in isolated Mn$^{\mathrm{III}}$. In $\mathrm{Mn^{II}Mn^{III}}$ complexes, which often exhibit weak exchange coupling,[23] the third term becomes important and can then be an additional source of anisotropy.

(50) Fiege, R. Paramagnetische Metallzentren im Photosystem II untersucht mit EPR/ENDOR Techniken. Doctoral thesis, Technische Universität, Berlin, 1997.

(51) Rieger, P. H. *Electron Spin Resonance*, Vol. 13B; The Royal Society of Chemistry: Cambridge, U.K., 1993; p 178.

(52) Margenau, H.; Murphy, G. M. *The Mathematics of Physics and Chemistry*, 2nd ed.; Van Nostrand: New York, 1955.

(53) Press, W. H.; Flannery, B. P.; Teukolsky, S. A.; Vetterling, W. T. *Numerical Recipes*; Cambridge University Press: Cambridge, U.K., 1986.

(54) Möbius, K.; Lubitz, W. In *Biological Magnetic Resonance*; Berliner, L. J., Reuben, J., Eds.; Plenum Press: New York, 1987; Vol. 7, p 129.

(55) Slichter, C. P. *Principles of Magnetic Resonance*, 3rd ed.; Solid-State Science 1; Springer: Berlin, 1990.

(56) Rist, G. H.; Hyde, J. S. *J. Chem. Phys.* **1970**, *52*, 4633.

(57) Flanagan, H.; Singel, D. J. *J. Chem. Phys.* **1987**, *87*, 5606.

(58) Britt, R. D.; Sauer, K.; Klein, M. P.; Knaff, D. B.; Kriauciunas, A.; Yu, C.-A.; Yu, L.; Malkin, R. *Biochemistry* **1991**, *30*, 1892.

(59) Britt, R. D.; Zimmermann, J.-L.; Sauer, K.; Klein, M. P. *J. Am. Chem. Soc.* **1989**, *111*, 3522.

$$\nu_+ = (3 + \eta)K \tag{13}$$

$$\nu_- = (3 - \eta)K \tag{14}$$

$$\nu_0 = 2\eta K \tag{15}$$

$$\nu_{dq} = 2\left[\left(\nu_{^{14}N} + \frac{1}{2}|A|\right)^2 + K^2(3 + \eta^2)\right]^{1/2} \tag{16}$$

To avoid "blind spots" in ESEEM spectra, two-dimensional data sets were recorded. After a Fourier transformation in the T dimension, one-dimensional spectra were obtained by performing a light projection along τ (see Figure 12).

2.11. Point-Dipole Model. The basic point-dipole model[60] can be adapted to describe the dipolar hyperfine coupling of a proton to the two electron spin centers in an exchange-coupled dinuclear complex.[33] The extension of this model, developed in our laboratory, enabled us to calculate the principal values of the hyperfine couplings analytically by summation over the individual hfc tensors.[37] Its main purpose is to find the location of a proton for a given dipolar hyperfine coupling tensor;[37] similar approaches have been used in refs 36 and 61. In this work, we use this model to predict the value of the tensor and compare it to the experimentally obtained one, thereby assigning proton positions known from the X-ray structure analysis to dipolar hyperfine coupling tensors.

In contrast to earlier models (e.g., ref 33), in which the problem is solved numerically, here the dipolar tensor is calculated by the analytical equation

$$\mathbf{A}^H = g_e\beta_e g_n\beta_n \cdot \mathrm{diag}(-\delta, -\Gamma + \delta/2, \Gamma + \delta/2)\ \mathrm{MHz\ Å^3} \tag{17}$$

with δ and Γ determined by the parameters r_1, r_2, and θ given in Figure 2.

$$\delta = 2{r_1}^{-3} - {r_2}^{-3}; \quad \Gamma = \frac{3}{2}\sqrt{4{r_1}^{-6} - 4{r_1}^{-3}{r_2}^{-3}\cos 2\theta + {r_2}^{-6}} \tag{18}$$

In general, the resulting tensor $\mathbf{A^H}$ is a *non*axial tensor. However, when the proton is located on the line joining the two Mn ions ($\theta = n\pi$), an axial tensor is obtained.

For practical use, the above equation can be modified (see also ref 36). We chose as relevant parameters the constant Mn−Mn distance d, the distance $Mn^{III}-H$, r_1, and the angle Φ between the vector $\vec{r}_1$ and the Mn−Mn vector $\vec{d}_1$. The parameters r_2 and Θ in eq 18 are then

$$r_2 = \sqrt{d^2 - 2dr_1\cos\Phi + {r_1}^2} \tag{19}$$

$$\Theta = \arcsin\frac{d}{r_2}\sin\Phi \tag{20}$$

The extended point-dipole model is applicable only if the distance between the magnetic moments is large compared with the size of the spin density distribution. Therefore, one must be careful when dealing with protons in the direct surrounding of the manganese ions. Nevertheless, this model is very helpful in correlating hyperfine coupling tensors to proton positions in the structure.

3. Results and Discussion

3.1. Synthesis and Physical Properties of Complexes. When a methanolic solution of dtne is treated with $[(Mn^{III})_3(OH_2)_3(\mu\text{-}O)(\mu\text{-}OAc)_6]OAc$ (manganese(III) acetate) and $NaClO_4$, a red solution forms from which red crystals of $[dtne_4Mn^{III}_8(\mu\text{-}O)_4(\mu\text{-}OAc)_8](ClO_4)_8$ can be isolated. The structure of this cyclic octanuclear complex will be published elsewhere. Addition of a few drops of water to a solution of this complex in acetonitrile initiates a disproportionation reaction which can be followed by a color change from red to green. Crystals of the resulting complex **1** are obtained by adding $NaBPh_4$. If the methylated derivative $(CH_3)_4$dtne is reacted with manganese(III) acetate under the same conditions, a green solution is formed directly. Here, complex **2a** or **2** is isolated by additon either of $NaClO_4$ or $NaBPh_4$. If an aqueous solution of **2a** is treated with perchloric acid, a color change from green to brown is observed, followed by the precipitation of complex **3** in about 70% yield. The pH dependency of this process can be understood as follows. The disproportionation reaction is induced by a protonation of a bridging oxo group of **2a**. The protonated species $H(\mathbf{2a})^+$ is a stonger oxidant than **2a**, yielding **3** and a protonated $Mn^{III}Mn^{III}$ intermediate, which is unstable and further disproportionates to **3** and a manganese(II) complex as the final products. This reaction is responsible for a certain amount of Mn^{II} impurities which can be identified spectroscopically and magnetically in all samples. The oxidized complex **3** and the reduced compound $[(CH_3)_4dtneMn^{III}_2(\mu\text{-}O)_2(\mu\text{-}OAc)]^+$ are also accessible electrochemically by controlled potential coulometry of the mixed-valent complex **2a**. The cyclic voltammogram in acetonitrile (0.1 mol/L $[n\text{-}Bu_4N]PF_6$/acetonitrile) shows a reversible one-electron oxidation at +0.68 V and reversible reduction at −0.35 V referenced versus NHE.

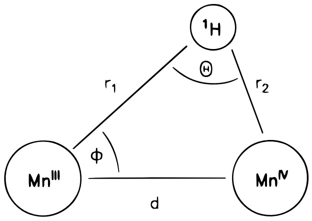

Figure 2. Schematic representation of the geometric parameters used in the point-dipole model (for details, see text).

Magnetic susceptibility studies in the temperature range of 2−300 K yielded coupling constants of −110, −112, and −100 cm^{-1} for **1**−**3**, respectively ($g = 2.00$ for Mn^{III} and Mn^{IV}, $D = 0$, $TIP = 0$)[62] using the usual spin Hamiltonian $H = -2JS_1S_2$.

3.2. Crystal Structures. The structures of complexes **1**, **2**, and **3** have been determined by X-ray crystallography. Crystal structures of **4**, **5**, and **6** have already been published.[41,63,64] Tables of atomic coordinates, distances, angles, and anisotropic displacement parameters are summarized in the Supporting Information. Figure S1 (given in the Supporting Information) shows the structure of the dication of **1** as an example for the three complexes containing the binucleating ligand dtne and its methylated derivative. The manganese ions are approximately in an octahedral environment, consisting of three nitrogen donor atoms of the macrocycle, two bridging oxo atoms, and a bridging acetate. The Mn−Mn distances of the acetato bridged complexes are at 2.553(1), 2.574(2), 2.599(4), and 2.588(2) Å for **1**−**4**, respectively. The reported metal−metal distances for the bpy and phen complexes **5** and **6**, bridged by only two oxo atoms, are significantly longer (for $(\mathbf{5})(ClO_4)_3 \cdot 3H_2O$ it is 2.716(2) Å, and for $(\mathbf{6})(PF_6)_3 \cdot MeCN$ it is 2.700(1) Å).[63,64] The Mn−O and Mn−N distances in **1** are clearly different for Mn(1) and Mn(2), as expected for a mixed-valent complex of class II according to the classification of Robin and Day.[65] The

---

[60] Weil, J. A.; Bolton, J. R.; Wertz, J. E. *Electron Paramagnetic Resonance, Elementary Theory and Practical Applications*; John Wiley: New York, 1994.

[61] Willems, J. P.; Lee, H.-I.; Burdi, D.; Doan, P. E.; Stubbe, J.; Hoffman, B. M. *J. Am. Chem. Soc.* **1997**, *119*, 9816.

[62] *TIP* = temperature-induced paramagnetism; *D* = zero-field parameter.

[63] Stebler, M.; Ludi, A.; Bürgi, H. B. *Inorg. Chem.* **1986**, *25*, 4743.

[64] Jensen, A. F.; Su, Z.; Hansen, N. K.; Larson, F. K. *Inorg. Chem.* **1995**, *34*, 4244.

[65] Robin, M. B.; Day, P. *Adv. Inorg. Chem. Radiochem.* **1967**, *10*, 247.

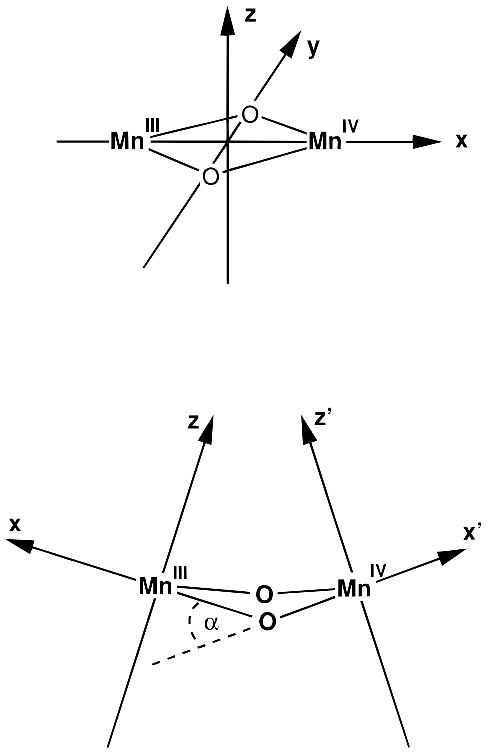

Figure 3. Schematic representation of the $Mn^{III}(\mu\text{-}O)_2Mn^{IV}$ core in complexes **1**, **2**, and **4** (bottom) and **5** and **6** (top). The coordinate systems that were used to correlate the **g** and hf tensors to the molecular structures are indicated.

octahedral axis O(4)−Mn(1)−N(1), standing perpendicular to the Mn_2O_2 plane, is about 0.28 Å longer than the corresponding axis O(3)−Mn(2)−N(4). The equatorial $Mn-O_{oxo}$ distances for Mn(1) are 1.78 Å; they are 0.05 Å shorter for Mn(2). This is in perfect agreement with the expected Jahn−Teller distortion of the high-spin manganese(III) ion, Mn(1), forming a stretched octahedron and the smaller ionic radius of the manganese (IV) ion, Mn(2). The structural parameters of **2** do not allow crystallographic distinction between the Mn^{III} and Mn^{IV} coordination sites of the cation. This is due to statistical disorder, which has been observed in several X-ray studies of mixed-valent, almost C_{2v} symmetric metal complexes, e.g., in **4** and **6**. The very large anisotropic displacement parameters of the ethylene carbon atoms in **2** are also indicative of this fact. The Mn−O and Mn−N distances are the arithmetic average of the distances found in **1**.

3.3. EPR. X- and Q-band EPR spectra were obtained from complexes **1**−**6**. In complex **3**, a $Mn^{IV}Mn^{IV}$ species, the antiferromagnetic exchange coupling leads to an effective electron spin $S_{eff} = 0$ ground state. Thus, this complex is EPR silent. Spectra of **2** and **6** are shown in Figures 4 and 5 as an example. The spectra could only be observed at low temperatures (below 100 K) and arise from the spin ground state for antiferromagnetically coupled $Mn^{III}Mn^{IV}$ complexes ($S = {}^1/_2$). In all cases, the exchange coupling is strong. Values of J for **1**−**3** are given above; for **4**−**6**, published values are −110,[41] −150,[17] and −134 cm^{-1},[17] respectively ($H = -2JS_1S_2$). All EPR spectra are of the “16-line” type, similar to those reported for mixed-valent $Mn^{III}Mn^{IV}$ complexes by other groups.[8,17,23,27,66,67]

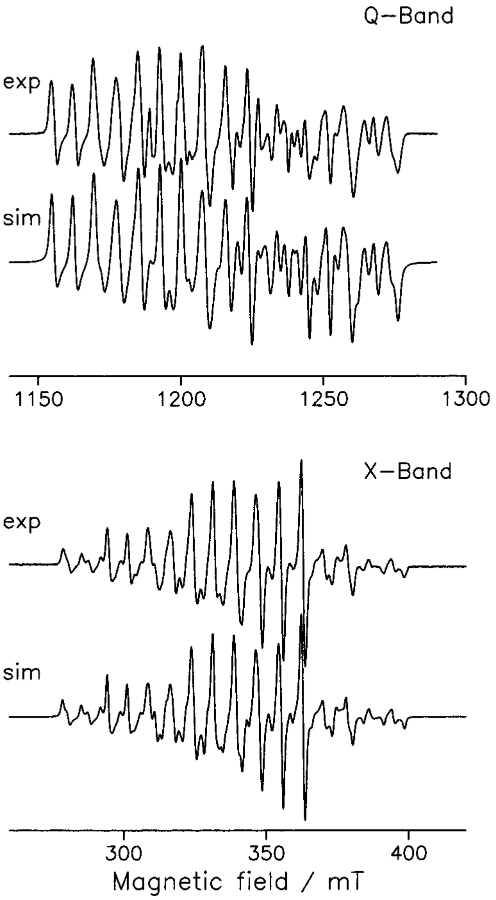

Figure 4. EPR spectra of model complex **2** in DMF. Experimental data are as follows. X-band: microwave frequency (ν_{MW}), 9.49 GHz; microwave power (P_{MW}), 2 mW; field modulation (FM), 12.5 kHz; amp., 0.1 mT_{pp}; T, 2.4 K; concentration, 1×10^{-3} mol/L; accumulation time, 2 min; time constant, 40 ms. Q-band: ν_{MW}, 34.2 GHz; P_{MW}, 12.9 μW; FM, 12.5 kHz; amp., 0.1 mT_{pp}; T, 50 K; concentration, 1×10^{-4} mol/L; accumulation time, 33 min; time constant, 160 ms. The simulations for X- and Q-band were performed with the data set given in Table 2; Gaussian line width, 0.6 mT (X-band) and 0.8 mT (Q-band). The same field scale is used for X- and Q-band spectra.

Due to **G** and hyperfine anisotropy, some lines exhibit further splittings and additional shoulders, especially at Q-band frequencies. Note that 16 lines are expected only for the case of identical intrinsic hfc’s of the Mn ions in the high-field limit. For couplings of about 16 mT, which equals the effective Mn^{III} hfc in the complexes, even at Q-band frequencies the high-field condition is not fulfilled, and second-order effects complicate the spectra. Recently, W-band (94 GHz) EPR spectra were obtained from **1** and **4**,[68,69] where such effects are fairly small and, due to the increased Zeeman splitting, show better separation between **G** and hf anisotropy.

Comparing Figures 4 and 5, the difference between the two classes of complexes becomes apparent. We can distinguish systems with μ-oxo bridges only (**5** and **6**) and complexes with μ-oxo-μ-acetato bridges (**1**, **2**, and **4**). At X-band frequencies, the spectra of **5** and **6** exhibit a total width of 127 mT, while spectra of **1**, **2**, and **4** are considerably narrower (117 mT). At Q-band frequencies, the widths are 130 and 118 mT, respectively.

---

(66) Diril, H.; Chang, H. R.; Nilges, M. J.; Zhang, X.; Potenza, J. A.; Schugar, H. J.; Isied, S. S.; Hendrickson, D. N. *J. Am. Chem. Soc.* **1989**, *111*, 5102.

(67) Frapart, Y.-M.; Boussac, A.; Albach, R.; Anxolabéhère-Mallart, E.; Delroisse, M.; Verlhac, J.-B.; Blondin, G.; Girerd, J.-J.; Guilhem, J.; Cesario, M.; Rutherford, A. W.; Lexa, D. *J. Am. Chem. Soc.* **1996**, *118*, 2669.

(68) Schäfer, K.-O.; Hofbauer, W.; Bittl, R.; Lubitz, W. In *Magnetic Resonance and Related Phenomena*; Ziessow, D., Lubitz, W., Lendzian, F., Eds.; TU Berlin: Berlin, 1998; Vol. II, p 863.

(69) Hofbauer, W.; Schäfer, K.-O.; Bittl, R. In *Magnetic Resonance and Related Phenomena*; Ziessow, D., Lubitz, W., Lendzian, F., Eds.; TU Berlin: Berlin, 1998; Vol. II, p 851.

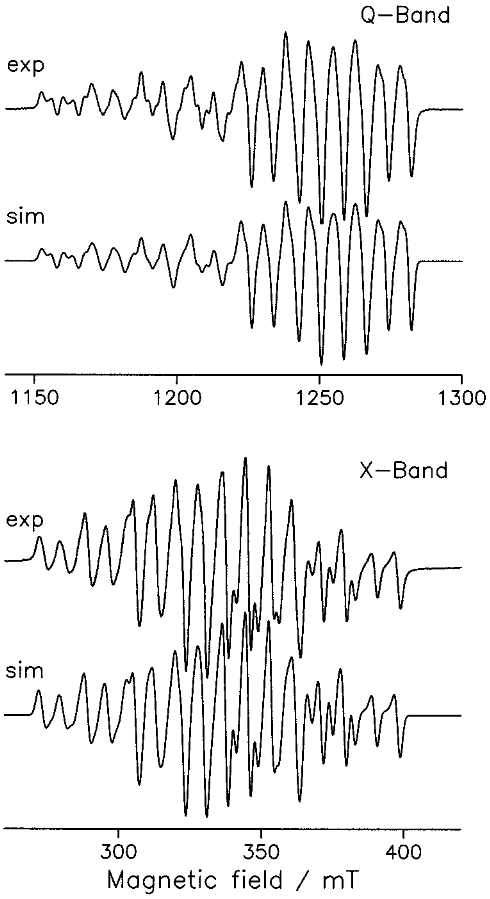

Figure 5. EPR spectra of model complex **6** in MeCN. Experimental data are as follows. X-band: ν_{MW}, 9.45 GHz; P_{MW}, 50 μW; FM, 12.5 kHz; amp., 0.2 mT_{pp}; *T*, 6 K; concentration, 1×10^{-3} mol/L; accumulation time, 17 min; time constant, 128 ms. Q-band: ν_{MW}, 34.01 GHz; P_{MW}, 80 μW; FM, 12.5 kHz; amp., 0.5 mT_{pp}; *T*, 50 K; concentration, 1×10^{-3} mol/L; accumulation time, 6 min; time constant, 82 ms. The simulations for X- and Q-band were performed with the data set given in Table 2; Gaussian line width, 0.9 mT (X- and Q-band). The same field scale is used for X- and Q-band spectra.

To extract the **G** and ^{55}Mn hf tensors from the spectra, it is necessary to perform computer simulations. To find a consistent set of parameters, simulations were carried out for two microwave frequencies, since the use of only one frequency can easily lead to erroneous data.[8] At X-band, line separations due to hyperfine splittings are 4 mT, and those due to **G** anisotropy are 3 mT. At Q-band frequencies, the **G** anisotropy is increased and becomes dominant. Furthermore, second-order hyperfine coupling effects are smaller.

For complexes **1**, **2**, and **4** with μ-acetato-bis-μ-oxo-bridges, a collinear axis system for **G** and hyperfine tensors was used. Spectra of complexes **5** and **6** with a bis-μ-oxo bridge gave the best results with Euler angle $\beta = \pm 8°$ for both hf tensor systems. Thereby, the *z*-axes of the hf tensor systems are rotated by this amount with respect to the **G** tensor system.

Table 2. **G** and Mn^{III} and Mn^{IV} Hyperfine Tensor Principal Values for the Binuclear Complexes[a]

complex	g	$\mathbf{A}^{III}$ (mT)	$\mathbf{A}^{IV}$ (mT)	g_{iso}	A^{III}_{iso} (mT)	A^{IV}_{iso} (mT)
1	*x* 1.997	−16.8	7.0			
	y 2.001	−14.8	7.8	1.994	−14.1	7.5
	z 1.983	−10.7	7.7			
2	*x* 1.996	−17.2	6.9			
	y 2.001	−15.1	7.9	1.993	−14.5	7.5
	z 1.983	−11.1	7.7			
4	*x* 1.999	−16.5	7.2			
	y 2.001	−15.0	7.7	1.995	−14.0	7.6
	z 1.985	−10.6	8.0			
5	*x* 1.992	−17.3	7.7			
	y 1.998	−18.0	7.6	1.991	−16.4	7.8
	z 1.982	−13.8	8.2			
6	*x* 1.992	−17.3	7.7			
	y 1.998	−17.8	7.5	1.990	−16.0	7.9
	z 1.980	−13.0	8.4			

[a] The tensor components were obtained from a simultaneous fit of X- and Q-band EPR spectra, see text. Errors: $\Delta g = \pm 1 \times 10^{-3}$, $\Delta A^{III} = \pm 0.2$ mT, $\Delta A^{IV} = \pm 0.1$ mT. The coordinate system chosen for all complexes (*x*, *y*, *z*) is shown in Figure 3 (top).

To account for unresolved hyperfine splittings of the coordinated nitrogen and hydrogen nuclei, a Gaussian line shape was used in the simulations. The line width was kept constant for all orientations and for all Mn m_I transitions. It is obvious from Figures 4 and 5 that good results were obtained under these assumptions. Only complex **5** behaves somewhat differently. Small structures in the center part of the Q-band spectrum could be reproduced by using a line width of 0.7 mT, while at the outer parts 0.9 mT was more adequate. To keep the number of fit parameters as small as possible, a line width dependence of the individual m_I transitions was not incorporated in the simulation, even though the simulations could be improved in this way, especially the spectral simulations of complex **5** at Q-band.

The differences between the experimental and simulated spectra were very small. The data for the principal **G** and ^{55}Mn hf tensor values obtained by this procedure are shown in Table 2 for the different complexes. Recently, complexes **1** and **4** have also been measured at W-band frequencies in our laboratory. A simulation of the spectra with the values from Table 2 gave very satisfactory results.[68] This shows that the obtained data set yields consistent results in three frequency bands and can, therefore, be considered to be reliable.

3.3.1. G Tensors. Using the vector projection model of spin coupling,[26,47] we will now explain the experimentally found values of the **g** tensors and establish a correlation between the tensor axes and the molecular structure. The molecular coordinate system for our complexes is chosen as shown in Figure 3 (top), see ref 70: the *x*-axis is along the line connecting the two Mn ions, the *y*-axis connects the two μ-oxygen atoms and the *z*-axis is perpendicular to the plane defined by Mn^{III}, O, O′, and Mn^{IV}.

We start with the separate manganese ions. For Mn^{III} in TiO_2 with its d^4 configuration, an axial **g** tensor with $g_\perp = 2.00 \pm 0.02$ and $g_\parallel = 1.99 \pm 0.01$ has been measured; the zero-field splitting parameters given are $D = -3.4 \pm 0.1$ cm^{-1} and $E = 0.116 \pm 0.001$ cm^{-1}.[71] Recent data by Barra et al.[72] were collected from a polycrystalline Mn^{III} complex. The values for the **g** tensor and zfs parameters are $g_\perp = 1.99$, $g_\parallel = 1.97$, $D = -4.35$ cm^{-1}, and $E = 0.26$ cm^{-1}. In isolated Mn^{III}, the single unpaired spin of Mn^{III} occupies the d_{z^2} orbital. This is also assumed in our model complexes.[32] This defines the axial direction in the complexes, which is orthogonal to the plane of the manganese and the μ-oxo atoms. This *z*-direction has the smallest *g* value according to ref 71.

For Mn^{IV}, a wide variety of data exist which were taken in various host crystals, yielding $g_{iso} = 1.994$ in octahedral

---

(70) Gamelin, D. R.; Kirk, M. L.; Stemmler, T. L.; Pal, S.; Armstrong, W. H.; Penner-Hahn, J. E.; Solomon, E. I. *J. Am. Chem. Soc.* **1994**, *116*, 2392.

(71) Gerritsen, H. J.; Sabisky, E. S. *Phys. Rev.* **1963**, *132*, 1507.

(72) Barra, A. L.; Gattechi, D.; Sessoli, R.; Abbati, G. L.; Cornia, A.; Fabretti, A. C.; Uytterhoeven, M. G. *Angew. Chem.* **1997**, *109*, 2423.

environments as in MgO,[73] $g_{\mathrm{iso}} = 1.9737$ in tetragonal distorted ligand spheres, as in Al_2O_3,[74,75] and in a rhombically distorted octahedral environment, measurements were done in TiO_2[76] and SnO_2.[77] From et al.[77] obtained principal values of $g_1 = 1.9879$, $g_2 = 1.9870$, and $g_3 = 1.9909$ (all values ±0.0003), and zero-field parameters are $D = 0.8818 \pm 0.0003\ \mathrm{cm}^{-1}$, $E = 0.2635 \pm 0.0003\ \mathrm{cm}^{-1}$. We will use the latter data given by From et al.[77] in our analysis. For the assignment of the **g** and hf tensor axes, see refs 71 and 77. To correlate the **G** tensor with the structure, we assign the unique axis of $\mathbf{g^{III}}$ (smallest value) to the molecular *z*-axis. This is resonable, because filling the d_{z^2} orbital removes the equivalence of the t_{2g} orbitals and therefore defines a unique axis. The axis system for $\mathbf{g^{IV}}$ is defined in such a way that the unique axis coincides with the *x*-axis of $\mathbf{g^{III}}$. The arguments are as follows: the energy of the manganese t_{2g} orbitals has been discussed in detail by Gamelin et al.[70] and by Zhao et al.,[78] who performed density functional calculations. The overall interaction between metal t_{2g} and μ-oxygen orbitals is strongest in the *x*-direction. Thus, the greatest distortion from spherical symmetry found in a pure octahedral crystal field is expected in the *x*-direction. We assume that this is the axis with the largest Mn^{IV} intrinsic **g** tensor component ($\mathbf{g^{IV}}$).

Complexes **1**, **2**, and **4** have an additional μ-OAc bridge which introduces a twist angle α between the two planes spanned by $Mn^{III}(\mu\text{-}O)_2$ and $Mn^{IV}(\mu\text{-}O)_2$ (see Figure 3, bottom, e.g., 19° in **1**). In these complexes, the two intrinsic **g** tensors are diagonal in different axis systems. When using eq 3, both intrinsic **g** tensors have to be transformed to a common axis system before the summation is done. When we neglect the zfs, the **G** tensor components can be calculated analytically (see Appendix for details). In this case, deviations from the exact formula are in the order of 10^{-4}, which is smaller than the error margin for the intrinsic manganese data. The isolated spin systems are then combined using eq 3. With the data of Gerritsen and Sabisky[71] and From et al.,[77] the principal values of the **G** tensor in the binuclear $Mn^{III}Mn^{IV}$ complexes are calculated to be $G_x = 2.01$, $G_y = 2.01$, and $G_z = 1.99$ for both $\alpha = 0°$ in **5** and **6** and $\alpha = 19°$, e.g., in **1**. The large error margin in the intrinsic Mn^{III} data obscures a nonaxiality of the calculated **G** tensors expected for the crystallographically determined angle α in **1**. The experimental **G** tensors are rhombic (Table 2) and somewhat smaller in magnitude for both classes of complexes. The rhombicity of the obtained **G** tensors can arise from a misalignment of the unique axes for two axially symmetric intrinsic **g** tensors $\mathbf{g^{III}}$ and $\mathbf{g^{IV}}$ or from at least one rhombic intrinsic tensor (most likely $\mathbf{g^{III}}$). We were not able to achieve good simulations using only axial tensors. Axial tensors may yield satisfactory results at X-band frequencies, but at Q-band and higher frequencies these are not sufficient.[68] Measurements by Zheng et al.[23] on complex **5** also yielded rhombic *g* values in very good agreement with the data presented here. A correlation between tensor axes and structure was, however, not done by these authors.[23]

The above analysis allowed us to find a relationship between the coordinates of the **G** tensor and the atomic coordinates of the model complexes. The *z*-axis has already been identified as the axis perpendicular to the $Mn^{III}(\mu\text{-}O)_2Mn^{IV}$ plane. The **G** tensor component along this direction has the smallest value. The *x*-axis connects the two manganese atoms, and the *y*-axis connects the two μ-oxygen atoms (Figure 3, top). The largest component of the **G** tensor is then lying along the *y* axis. The intermediate component is found for the *x*-axis in the model complexes.

3.3.2. ^{55}Mn Hyperfine Couplings. The ^{55}Mn hyperfine tensors will now be correlated with the molecular structure in a similar way as the **G** tensor. For the intrinsic Mn^{III} hfc's, the data of Gerritsen and Sabisky[71] are the only data available. These authors found a rhombic hf tensor with principal values $a_1^{III} = 9.0 \pm 0.2$ mT, $a_2^{III} = 8.62 \pm 0.11$ mT, $a_3^{III} = 5.65 \pm 0.05$ mT for Mn^{III} in TiO_2. For Mn^{IV} in SnO_2, a rhombic hf tensor with principal values $a_1^{IV} = 7.77 \pm 0.05$ mT, $a_2^{IV} = 7.54 \pm 0.05$ mT, $a_3^{IV} = 8.064 \pm 0.05$ mT was given by From et al.[77] The axis systems were chosen as before, so that we have to transform both $\mathbf{d^{IV}}$ and $\mathbf{a^{IV}}$ to the axis system of Mn^{III}. Note that we use the exact formula (eqs 6 and 7) here because of the greater influence of the zfs on the hfc's. The principal values of the hf tensors could be found numerically using a computer program written in C. The principal values of hf tensors in the binuclear complexes with $J = -150\ \mathrm{cm}^{-1}$ (e.g., **5**) are calculated to be $A_x^{III} = -17.8$ mT, $A_y^{III} = -17.1$ mT, $A_z^{III} = -\ 11.5$ mT and $A_x^{IV} = 7.9$ mT, $A_y^{IV} = 7.4$ mT, $A_z^{IV} = 8.1$ mT. The hyperfine anisotropy is $\Delta A^{III} = A_{max}^{III} - A_{min}^{III} = 6.2$ mT and $\Delta A^{IV} = A_{max}^{IV} - A_{min}^{IV} = 0.7$ mT. With a weaker exchange coupling, $J = -110\ \mathrm{cm}^{-1}$ (e.g., complex **4**), we expect that somewhat more hyperfine anisotropy is transferred from Mn^{III} to Mn^{IV} than in complexes **5** and **6**. Indeed, we obtain $A_x^{III} = -17.7$ mT, $A_y^{III} = -17.1$ mT, $A_z^{III} = -11.6$ mT and $A_x^{IV} = 7.7$ mT, $A_y^{IV} = 7.4$ mT, $A_z^{IV} = 8.3$ mT. The anisotropies are $\Delta A^{III} = 6.1$ mT and $\Delta A^{IV} = 0.9$ mT.

The extent of anisotropy transfer from Mn^{III} to Mn^{IV} via zero-field splitting is described in ref 23. We calculated the anisotropy ΔA^{IV} for **5** without taking zfs into account to be 0.5 mT. Thus, the anisotropy transferred from $\mathbf{A^{III}}$ to $\mathbf{A^{IV}}$ via zfs is 0.2 mT. For complex **4**, the transferred anisotropy was calculated to 0.4 mT. The effect of the magnitude of the exchange coupling is clearly evident (cf. eqs 6 and 7): the less stronly coupled the system is, the more anisotropy is transferred for given $\mathbf{d^{III}}$ and $\mathbf{d^{IV}}$ values. Our calculations show that, in the Mn^{III} Mn^{IV} complexes investigated here, the major source of anisotropy is the intrinsic anisotropy of Mn^{III}. This is in agreement with ref 23. For comparison with the experimental data, the complexes can be divided into two classes, namely those with μ-oxo bridges (**5** and **6**) only and those with μ-oxo-μ-acetato bridges (**1**, **2**, and **4**). The former class shows strong correlation between **G** tensor and $\mathbf{A^{III}}$ tensor axes; the axes with the largest tensor components coincide. The same is found for the intermediate and the smallest component. For the $\mathbf{A^{IV}}$ tensor, the smallest component belongs to the same axis (*z*-axis) as the largest **G** tensor component. For all three tensors, the intermediate component is along the *x* -axis. In the second class (**1**, **2**, and **4**), the order of Mn^{III} hf tensor components is $x > y > z$, in contrast to the first class (**5** and **6**), where $y > x > z$ is found. The second class can be divided further into those with (**1** and **2**) and without (**4**) the connecting $-CH_2CH_2-$ fragment. In **1** and **2**, the *y* component for the $\mathbf{A^{IV}}$ tensors has the (absolute) largest value, while in **4** this is the *z* component. All complexes analyzed have their largest **G** tensor component on the same axis (*z*) as the largest $\mathbf{A^{III}}$ tensor component. The calculated tensor values showed the correct ordering for the $\mathbf{A^{III}}$ tensor components in **1**, **2**, and **4** (not for **5** and **6**), and for the $\mathbf{A^{IV}}$

---

(73) Nakada, M.; Awazu, K.; Ibuki, S.; Miyako, T.; Date, M. *J. Phys. Soc. Jpn.* **1964**, *19*, 781.

(74) Sierro, J.; Lacroix, R. *Helv. Phys. Acta* **1959**, 286.

(75) Geschwind, S.; Kisliuk, P.; Klein, M. P.; Remeika, J. P.; Wood, D. L. In *Paramagnetic Resonance*; Low, W., Ed.; Academic: New York, 1963; Vol. 1, p 113.

(76) Andresen, H. G. *J. Chem. Phys.* **1961**, *35*, 1090.

(77) From, W. H.; Dorain, P.; Kikuchi, C. *Phys. Rev. A* **1964**, *135*, 710.

(78) Zhao, X. G.; Richardson, W. H.; Chen, J.-L.; Li, J.; Noodleman, L.; Tsai, H.-L.; Hendrickson, D. N. *Inorg. Chem.* **1997**, *36*, 1198.

tensors the ordering was predicted correctly in **5** and **6** (not for **1**, **2**, and **4**). The more symmetric complexes **5** and **6** show more similarities with the calculated tensors. The deviation observed can be due to the fact that either the intrinsic $\mathbf{a}^{III}$ and $\mathbf{a}^{IV}$ tensors are somwhat different for both classes of complexes or the TiO_2 or SnO_2 host lattices in which the isolated ions have been measured are not good models for our $Mn^{III}Mn^{IV}$ complexes, which were measured in frozen organic solvents.

Comparison of our experimental data for complex **5** (Mn^{III}, $A_x = -485 \pm 6$ MHz, $A_y = -504 \pm 6$ MHz, $A_z = -387 \pm 6$ MHz; Mn^{IV}, $A_x = 216 \pm 3$ MHz, $A_y = 213 \pm 3$ MHz, $A_z = 230 \pm 3$ MHz) with published data shows a very good agreement.[23] For this complex, ^{55}Mn ENDOR experiments have been performed by Randall et al.,[35] who found axial hf tensor values (Mn^{III}, $A_\perp = -480$ MHz, $A_\| = -360$ MHz; Mn^{IV}, $A_\perp = 212$ MHz, $A_\| = 231$ MHz) within excellent numerical agreement for Mn^{IV}; the $A_\perp^{III}$ compares well with our A_x^{III} component, while our A_z^{III} is somewhat larger than the $A_\|^{III}$ measured in ref 35. Hyperfine tensor axes have not been assigned by Randall et al.[35]

To support the Mn hf tensor values obtained from the EPR simulations, ^{55}Mn cw-ENDOR experiments have been performed on complexes **1**, **2**, and **4**.[25,79] Such experiments yield, in principle, directly the ^{55}Mn hf and quadrupole tensor components.[25] The Mn^{III} and Mn^{IV} regions are well separated since $|\mathbf{A}^{III}| \approx |2\mathbf{A}^{IV}|$. The ^{55}Mn cw-ENDOR spectra are, indeed, split into two regions. The Mn^{IV} resonances are found in a rather small range from 80 to 100 MHz, and the Mn^{III} resonances are distributed over a broad region between 140 and 235 MHz, in agreement with the larger hf anisotropy of Mn^{III} (see Table 2). The ranges for the two tensors have been confirmed by ENDOR-induced-EPR (EIE) experiments.[30] EIE signals could only be obtained in the region between 80 and 100 MHz and between 140 and 235 MHz. For Mn^{III} and Mn^{IV}, the ENDOR linewidths are about 8 and 2 MHz, respectively. From theory, a maximum of 10 lines per manganese ion is expected. Since only unresolved lines are observed, we conclude that the quadrupole splitting is smaller than the linewidths (8 MHz). The environment of the manganese ions is rather symmetrical (octahedral), and small values are, therefore, not surprising. Randall et al.[35] reported some quadrupole couplings for complex **5** using pulsed ENDOR techniques, which are, indeed quite small (Mn^{III}, $P_\| = 4.5$ MHz, $\eta = 0.1$; Mn^{IV}, $P_\perp = 2$ MHz, $\eta = 0.3$). In conclusion, our data from the ^{55}Mn cw-ENDOR spectra fully support the magnitude and anisotropy of the respective data obtained from EPR simulations (Table 2). Furthermore, it is, in principle, possible to find a correlation between the tensor axes and the molecular structure using the vector projection model and a transformation of the intrinsic **g** and hyperfine tensors of Mn^{IV}.

3.4. ^{1}H cw-ENDOR. In Figure 6, ENDOR spectra of complexes **1**, **2**, and **4** are shown. All spectra were recorded at about 2 K. Only at these low temperatures is it possible to saturate the EPR transitions necessary for cw-ENDOR experiments. Most of the lines are symmetrically spread about the ^{1}H Larmor frequency, although some strong resonances are also observed in the low-frequency range without any counterparts at high frequencies. The spectra were obtained for various positions of the EPR line pattern. Apart from some minor intensity changes, the field setting on the inner lines of the EPR spectra did not change the position of lines relative to ν_n, i.e., the hyperfine splittings remained the same. Figure 7 shows an example of two spectra taken at different field positions. Here, the proton hyperfine lines could be well distinguished from the ^{14}N resonances on the basis of their different shift of Larmor frequencies, which are $\nu_{^1H} = 13.67$ MHz and $\nu_{^{14}N} = 0.99$ MHz at 321 mT and $\nu_{^1H} = 14.31$ MHz and $\nu_{^{14}N} = 1.03$ MHz at 336 mT (see eqs 9 and 11).

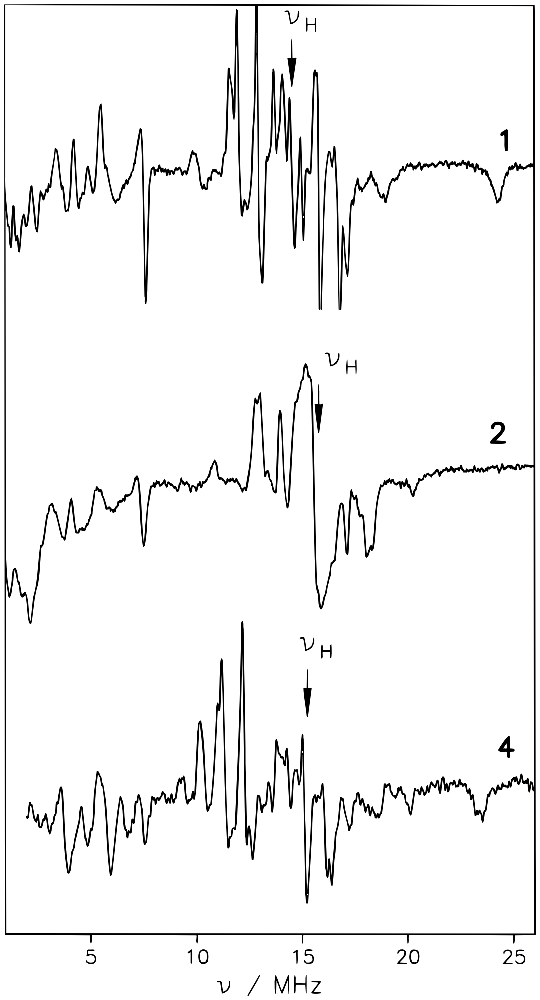

Figure 6. ENDOR spectra of model complexes **1**, **2**, and **4** in DMF. Experimental data: ν_{MW}, 9.44 GHz; FM, 1.56 kHz; amp., 50 kHz; *T*, 2 K; time constant, 320 ms; acummulation time (averaged), 30 min. For **1**: field, 322.4 mT; P_{MW}, 20 mW; radio frequency power (P_{RF}), 20 W. For **2**: field, 364.3 mT; P_{MW}, 4 mW; P_{RF}, 20 W. For **4**: field, 336.0 mT; P_{MW}, 4 mW, P_{RF}, 100 W.

The proton ENDOR spectra of all our model complexes show line pairs belonging to at least five different hyperfine tensors, and they exhibit the shape typically found for rhombic tensors in powders (see below). Due to the higher symmetry of **5** and **6**, many hf tensors are similar. Therefore, the resolution in these spectra is lower compared with that of **1**, **2**, and **4**. Furthermore, many lines resulting from small hf coupling tensors lead to a poorly resolved region around the matrix peak (not shown). From the intensities, it is not obvious how many different types of protons contribute to the ENDOR pattern. For all model complexes, the experimentally observed hf splittings are summarized in Tables 3 and 4.

Figure 6 shows that the largest splittings, corresponding to a hf tensor component of approximately 20 MHz, found in **1** and **4** are missing in **2**. Closer analysis also reveals that a component of 8.8/8.7 MHz is present in **1** and **4** but not in **2**. From structural similarities, it can be concluded that these components belong to the NH protons bound to N2, N3, N5, and N6. These protons

---

(79) Lubitz, W.; Zweygart, W.; Bittl, R.; Wieghardt, K.; Haselhorst, G.; Weyhermüller, T. In *Bioinorganic Chemistry—Transition metal ions in biology and their coordination chemistry*; Trautwein, A. X., Ed.; Wiley-VCH: New York, 1997; p 665.

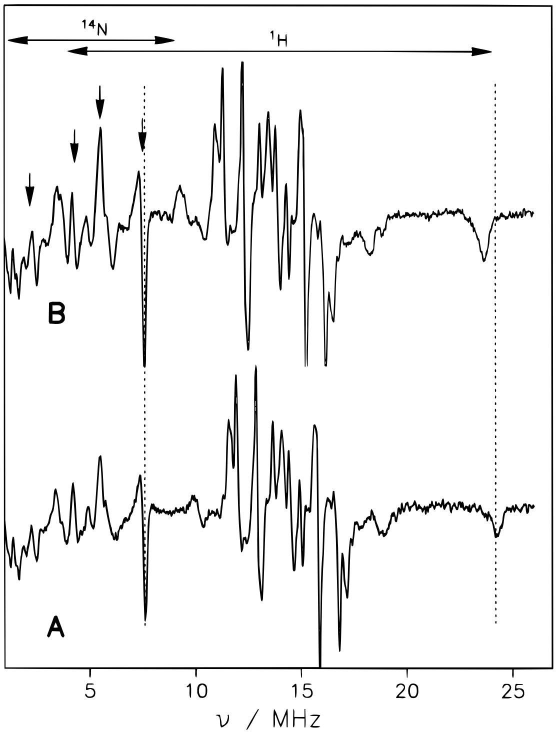

Figure 7. ENDOR spectra of complex **1** in DMF recorded at two different field positions to distinguish ^{1}H from ^{14}N lines. Field: 321.3 (B) and 336.0 mT (A). For experimental conditions, see Figure 6. For spectrum A, the Larmor frequency is $\nu_{^1\mathrm{H}} = 14.4$ MHz. The respective $\nu_{^{14}\mathrm{N}} = 1.01$ MHz coincides with the start of the frequency sweep. Note the shift of ^{1}H ENDOR lines for the different field positions. Lines belonging to ^{14}N resonances are much less shifted (see vertical dotted lines for ^{14}N near 7.5 MHz and for ^{1}H near 24 MHz). In the ^{14}N range, four lines belonging to one large ^{14}N tensor (hf and quadrupole splitting) are indicated by arrows (see text for details). The counterpart of the rightmost ^{1}H ENDOR line is superimposed by ^{14} N lines and is, therefore, not easily seen.

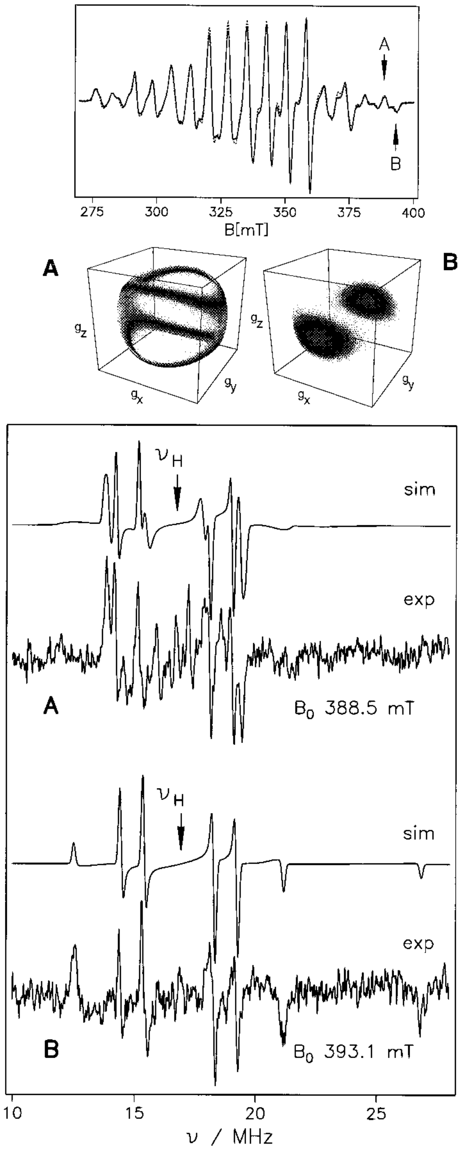

Figure 8. Orientation-selection ENDOR of model complex **1**. The EPR spectrum of **1** is shown on top. Field positions that were used to record the ENDOR spectra are indicated by arrows. Below, the molecular orientations that contribute to the ENDOR spectra at these positions are shown (A, 388.5 mT; B, 393.1 mT). Experimental data are as follows. A: field, 388.5 mT. B: field, 393.1 mT; ν_{MW}, 9.39 GHz; P_{MW}, 16 mW; P_{RF}, 20 W; FM, 1.56 kHz; amp., 50 kHz; *T*, 2 K; accumulation time, 1 h 43 min. The following hf tensors were used in the simulation of the orientation-selection ENDOR spectra: (1) $A_{\mathrm{iso}} = 3.17$ MHz, $\mathbf{A_{dip}} = (16.83, -8.87, -7.97)$ MHz; (2) $A_{\mathrm{iso}} = -1.58$ MHz, $\mathbf{A_{dip}} = (-7.07, 4.48, 2.59)$ MHz; (3) $A_{\mathrm{iso}} = 0$ MHz, $\mathbf{A_{dip}} = (5.84, -2.92, -2.92)$ MHz; and (4) $A_{\mathrm{iso}} = 0$ MHz, $\mathbf{A_{dip}} = (9.6, -4.8, -4.8)$ MHz.

could be exchanged by use of deuterated solvent. Thereby, the assignment of the splittings to the aforementioned protons could be verified. Other tensor components could not be identified by H/D exchange, leading to the conclusion that there is strong superposition with components of other hf tensors. The ENDOR spectrum of **4** further shows lines that are only found in this complex (Table 3). The respective tensor components are 18.9, 12.6, 11.7, 6.7, and 2.3 MHz and must result from protons bound to N1 and N4. This was concluded from a comparison with **1** and specific deuteration of these positions.

The CH_2CH_2 fragment that connects the tacn ligands is present in **1** and **2**. However, splittings that were found only in these complexes could not be resolved. One tensor component (7 MHz) of such a CH_2CH_2 proton was, however, identified by substitution of protons with deuterons. The ENDOR spectrum of **2** shows further splittings of 3.2, 1.9, and 1.6 MHz that were not present in **1** and **4**. The 1.9-MHz component could be assigned to NCH_3 protons by H/D substitution. Protons in the bridging OAc fragment were also replaced by deuterons. Here, a tensor component of 0.8 MHz could be identified in **1** and **4**. A change in the spectrum of **2** was not observed upon deuteration of OAc. This is most likely due to a superposition of other lines. The remaining spectral features are found in all three complexes and could not be assigned by H/D exchange. ENDOR spectra of **5** and **6** are almost identical since the structures are very similar. Differences are expected only for positions remote from the Mn ions ($d_{\mathrm{Mn-H}} \approx 7$ Å) and should, therefore, appear in the matrix region. Since this region is not well resolved in **5** and **6**, assignments are difficult. Specific deuterations within the ligands are not trivial and have not been done so far. Orientation-selection experiments and the extended point-dipole model were used in this case to assign the proton positions.

3.5. Orientation-Selection ENDOR. Orientation-selection ENDOR spectra of **1** and **2** were taken on the line at highest field positions in the EPR spectrum (see Figure 8). For **5** and **6**, this line was not selected since a better separation of perpendicular and parallel components could be obtained on the third line from the high-field end. As stated earlier, orientation selection was not possible for **4**. The ENDOR signal intensity obtained at those field positions was very weak. The

Table 3. Calculated and Experimentally Observed ^{1}H Hyperfine Splittings of Complexes **1**, **2**, and **4**

complex	calculated[a]			experimental[b]				assignment[c]
	A'_1	A'_2	A'_3	A_1	A_2	A_3	A_{iso}	
1	17	−9	−8	19.8	(−)5.6	(−)4.9	3.1	N2, N3
	−7	4	3	(−)8.7	2.9	1.3	−1.5	N5, N6
	8	−4	−4	9.3	(−)4.9	(−)4.9	0	C1a, C3a, C5a
	6	−3	−3	5.6	(−)2.9	(−)2.9	0	C1b, C3b, C5b, C2, C4, C6
	7	−5	−2	7.1	(−)4.9	(−)1.3	0	C7a
	5	−3	−2	4.9	(−)2.9	(−)1.3	0	C7b
	6	−5	−1	5.6	(−)4.9	(−)1.3	0	C8a
	3	−3	0	2.9	(−)2.9	0	0	C8b
	−4	3	1	(−)4.9	2.9	1.3	0	C9a, C11a, C13a
	−2	1	1	(−)2.9	1.3	1.3	0	C9b, C11b, C13b, C10, C12, C14
	2.3[d]	−1.6[d]	−0.7[d]	2.9	(−)1.3	(−)0.8	0	C16
2	8	−4	−4	9.3	(−)4.8	(−)4.8	0	C1a, C3a, C5a
	6	−3	−3	5.6	(−)2.8	(−)2.8	0	C1b, C3b, C5b, C2, C4, C6
	−4	3	1	(−)4.8	2.8	1.3	0	C9a, C11a, C13a
	−2	1	1	(−)2.8	1.3	1.3	0	C9b, C11b, C13b, C10, C12, C14
	7	−5	−2	7.6	(−)4.8	(−)2.8	0	C7a
	5	−3	−2	4.8	(−)2.8	(−)2.8	0	C7b
	6	−5	−1	5.6	(−)5.6	(−)1.3	0	C8a
	3	−3	0	2.8	(−)2.8	0	0	C8b
	2.3[d]	−1.6[d]	−0.7[d]	2.8	(−)1.6	(−)0.3	0	C16
	8.6[e]	−4.7[e]	−3.9[e]				0	C17, C18
	−3.5[f]	2.7[f]	0.8[f]				0	C19, C20
4	15	−9	−6	18.9	(−)6.7	(−)2.3	3.1	N1
	17	−9	−8	19.7	(−)5.3	(−)4.8	3.2	N2, N3
	−8	8	0	(−)12.6	11.7	(−)2.9	−1.3	N4
	−7	4	3	(−)8.8	2.9	1.3	−1.5	N5, N6
	8	−4	−4	9.3	(−)4.8	(−)4.8	0	C1a, C3a, C5a
	6	−3	−3	5.3	(−)2.9	(−)2.9	0	C1b, C3b, C5b, C2, C4, C6
	−4	3	1	(−)4.8	2.9	1.3	0	C9a, C11a, C13a
	−2	1	1	(−)2.9	1.3	1.3	0	C9b, C11b, C13b, C10, C12, C14
	2.3[d]	−1.6[d]	−0.7[d]	2.9	(−)1.3	(−)0.3	0	C16

[a] Calculated dipolar part of tensor **A′**, from X-ray structure (H positions), using the extended point-dipole model. [b] From ENDOR, error ±0.2 MHz; signs were not determined experimentally but adapted from theory. Note that the isotropic part of the experimental tensor $A_{iso} = 1/3\mathrm{Tr}\mathbf{A}$ has to be subtracted from the A_i values for comparison with A'_i. All A_{iso} values ≤0.3 MHz were set to zero. [c] Assignment according to best fit between experimental observed and calculated results. Proton positions are given by the C/N atom that they are connected to (see Figure 1). Positions without lowercase letters refer to all hydrogens connected to the respective atom. See also Figure 10. [d] The dipolar tensor of the OAc protons in the μ-OAc bridge given here represents the average of 72 tensor values obtained by rotating the methyl group about the C−C axis. The principal tensor values for the methyl proton positions as given in the crystal structure are 2.5, −1.7, −0.8 MHz (for C16a, C16b) and 1.9, −1.6, −0.3 MHz (for C16c). [e] The tensor has been averaged (see note *d*). For the NCH_3 proton positions given in the crystal structure, the principal tensor values evaluate to 10.0, −5.5, −4.5 MHz (for C17a, C18a, C17b, C18b) and to 4.9, −2.6, −2.3 MHz (for C17c, C18c). [f] The tensor has been averaged (see note *d*). For the NCH_3 proton positions given in the crystal structure, the tensors evaluate to −4.5, 3.7, 0.7 MHz (C19a, C20a), to −4.0, 2.9, 1.1 MHz (for C19b, C20b), and to −1.7, 1.2, 0.5 MHz (for C19c, C20c).

spectra were simulated by our program for simulations of solid-state ENDOR spectra.[80] A problem is that **G** and hyperfine anisotropy are of similar magnitude in X-band. However, from our EPR simulation data, we were able to distinguish the **G** and hf tensor components that contribute to the individual EPR lines.

Experimental and simulated orientation-selection ENDOR spectra are shown in Figure 8 for **1** as an example, along with diagrams showing the selected subsets of molecules for the field positions indicated in the EPR spectrum. It can be seen that, for a field setting $B_0 = 393.1$ mT, only those molecules that have their g_y axis aligned with the magnetic field contribute to the ENDOR spectrum. For the other position, $B_0 = 388.5$ mT, the angular distribution is more complicated, since the **G** and both ^{55}Mn hf tensors affect the selection. In the simulation of the spectra, the relative orientation of the proton hf tensors and the **G** tensor is described by the Euler angles (α, β, and γ).

We could assign one tensor (19.8; (−) 5.6; (−) 4.9) MHz[81] to protons bound to N2, N3 on the Mn^{III} side and a second one ((−) 8.8; 2.9; 1.3) MHz to the respective protons on the Mn^{IV} side (N5, N6). Two other tensors (5.6; (−) 2.9; (−) 2.9) MHz and (9.6; (−) 4.8; (−) 4.8) MHz were assigned to protons attached to carbons within the tacn part of the ligand (for details, see Figure 8 caption). For these protons within tacn, orientation selection is the only way to experimentally assign tensor axes, since a specific deuteration has not been performed for the tacn. Similar results were obtained for the other complexes mentioned above.

3.6. Application of the Point-Dipole Model. The extended point-dipole model has proven to be a useful tool to estimate distances and bond angles in biological systems.[33,36,37,61] First we wish to outline some useful properties of this model.

Figure 9 illustrates how the point-dipole model can be used to locate protons if their dipolar hf tensor is known. The contour plots are two-dimensional cross sections through space. Contour lines are drawn for the tensors $\mathbf{A_H} = -0.4,-2.7,3.1$ MHz (top) and $\mathbf{A_H} = 0.5,-3.8,3.3$ MHz (bottom). The crosspoints of the three lines indicated by arrows give the spatial location of a proton with such a tensor. The solid line represents the contour line for the principal tensor component with a principal axis perpendicular to the paper plane.

Based on the extended point-dipole model, we have calculated the dipolar tensors for all protons attached to the ligands of the five complexes **1**, **2**, **4**, **5**, and **6**. This calculation was based on

---

(80) Gessner, C. NiFe Hydrogenasen. Beiträge der EPR-Spektroskopie zur Strukturaufklärung des aktiven Zentrums. Doctoral thesis, Technische Universität, Berlin, 1996.

(81) Signs were not determined experimentally but were adapted from the results of our point-dipole model.

Table 4. Calculated and Experimentally Observed ^{1}H Hyperfine Splittings of Complexes **5** and **6**

complex	calculated[a]			experimental[b]			assignment[c]
	A'_1	A'_2	A'_3	A_1	A_2	A_3	
5	10.0	−5.2	−4.8	9.8	(−)5.1	(−)4.4	C26, C36
	9.4	−6.2	−3.4	9.8	(−)6.2	(−)3.4	C16
	9.0	−5.8	−3.2	9.8	(−)6.2	(−)3.4	C46
	9.0	−7.7	−1.4	9.8	(−)7.9	(−)1.2	C86
	8.3	−7.3	−1.0	7.9	(−)7.9	(−)1.2	C56
	−3.9	2.4	1.5	(−)3.4	2.4	1.2	C66, C76
	2.0	−1.0	−1.0	2.4	(−)1.2	(−)1.2	C15, C25, C35, C45
	2.1	−1.1	1.0	2.4	(−)1.2	(−)1.2	C13, C23, C33, C43
	1.4	−1.1	−0.3	1.2	(−)1.2	(−)0.4	C55, C85
	1.2	−0.7	−0.5	1.2	(−)0.4	(−)0.4	C14, C24, C34, C44
	±0.2	±0.6	±0.8	±0.4	±0.4	±1.2	C53, C63, C73, C83, C54
	±0.8	±0.6	±0.4	±1.2	±0.4	±0.4	C64, C74, C84, C65, C75
6	10.5	−6.9	−3.6	9.0	(−)7.6	(−)3.0	C16
	10.0	−6.5	−3.5	9.0	(−)7.6	(−)3.0	C46
	9.8	5.0	−4.7	9.0	(−)5.8	(−)4.2	C36
	10.1	−5.3	−4.9	9.0	(−)5.8	(−)4.2	C26
	7.4	−6.5	−0.9	7.6	(−)5.8	(−)0.7	C56
	6.9	−6.1	−0.8	7.6	(−)5.8	(−)0.7	C86
	−3.9	2.3	1.5	(−)3.0	1.8	1.2	C66, C76
	2.0	−1.0	−1.0	1.8	(−)1.2	(−)1.2	C25, C35
	1.9	−1.1	−0.7	1.8	(−)1.2	(−)0.7	C15, C45
	1.3	−0.7	−0.6	1.2	(−)0.7	(−)0.7	C14, C24, C34, C44
	1.0	−0.6	−0.5	1.2	(−)0.7	(−)0.7	C17, C27, C37, C47
	1.3	−1.0	−0.3	1.8	(−)1.2	(−)0.2	C55, C85
	0.6	−0.5	−0.1	0.7	(−)0.7	(−)0.2	C84, C84
	0.3	−0.3	0.0	0.2	(−)0.2	0.0	C64, C65, C67, C57
	0.3	−0.3	0.0	0.2	(−)0.2	0.0	C74, C75, C77, C87

[a] Calculated dipolar part of tensor **A′**, from X-ray structure (H positions), using the point-dipole model. [b] From ENDOR, error ±0.2 MHz; signs were not determined experimentally but adapted from theory. The isotropic part $|A_{iso}|$ of the experimental tensor is smaller than 0.5 MHz in all cases. [c] Assignment according to best fit between experimentally observed and calculated results. Proton positions are given by the C/N atom that they are connected to (see Figure 1). See also Figure 11.

the known structures of these complexes (this work and refs 41, 63, and 64). The X-ray structures of **2**, **4**, and **6** show disorder so that no difference between Mn^{III} and Mn^{IV} is seen. This, however, leads to an additional error in the calculated dipolar hf tensors, because Mn^{III} is known to exhibit elongated axial bonds (Jahn−Teller distortion). To account for this, the calculated tensors in **2** and **4** are based on the X-ray structure of **1**. Deviations in substituents from complex **1** were compensated manually. The geometry at N1 and N4 in **4** was assumed to be perfectly tetrahedral; the protons were then added with an N−H bond length of 1.0 Å. The NCH$_3$ protons in **2** were added in a similar way. The positions of the NH protons in **1** could be determined directly from X-ray analysis. However, the couplings that were calculated using these values were too large (23 MHz). We therefore recalculated these hydrogen positions using tetrahedral geometry at N2, N3, N5, and N6, with $d_{N-H} = 1.0$ Å. For **6**, the coordinates given by Stebler et al.[63] were used to see how the inequivalence of Mn^{III} and Mn^{IV} alters the dipolar couplings as compared with those of **5**. It must be emphazied, though, that an error in the calculated hf tensors for **6** is thereby introduced.

The calculated values are given in Tables 3 and 4, together with the experimental hf tensors. Note that respective hf components have opposite signs when the protons are located on either the Mn^{III} or the Mn^{IV} side. The magnitude of the tensors is determined by the distance and exact position of the proton with respect to the Mn−Mn core. A feature that is common to complexes **1**, **2**, and **4** is the rotating CH$_3$ groups in the μ-acetato bridges. Complex **2** further has four NCH$_3$ groups that are subject to rotation. It is possible that we encounter a distribution of proton positions for these methyl groups in our frozen solutions. To account for this, we rotated the respective group in steps of 15° and calculated the dipolar tensor after each rotation. Due to the C_3 symmetry, 72 proton tensors were obtained for each methyl group. The averaged principal values are given in Table 3. The values one obtains when using the crystal structure positions are also given, since it can be assumed that these are the energetically most favorable positions.

3.7. Assignments of hfcs to Molecular Positions. Based on these calculations, all hyperfine splittings in the spectra were assigned to specific protons in the complexes. For those protons which could already be assigned by structural comparisons of the complexes and by specific ^{2}H labeling, the agreement with the assignment based on the point-dipole model is very good. The results are given in Tables 3 and 4. A visualization of the largest tensor component for each proton in complexes **4** and **5** is depicted in Figures 10 and 11.

For the NH protons that are very close to the Mn nuclei, a significant isotropic hfc must be assumed. This has, indeed, been obtained from the analysis of the experimental spectra (Figure 6, Table 3). The isotropic part of the hfc's is also indicated by comparing the calculated dipolar part with the experimentally observed hfc's. We further utilized the fact that the isotropic part on the Mn^{III} side is twice as large as the one on the Mn^{IV} side and has opposite sign. From the work of Tan et al.[32] on similar Mn^{III}Mn^{IV} complexes with nitrogen ligands, it can be assumed that some spin density (approximately 0.01−0.02) is transferred from the manganese to the axial nitrogen that leads to a rather large ^{14}N hfc. Hydrogens bound to these nitrogens should also show an isotropic hfc via either spin polarization or direct overlap with the nitrogen orbitals or directly with the manganese 3d orbitals. Equatorially bound nitrogens have a smaller isotropic hfc that can then be transferred to protons. A detailed analysis of these hfc's requires an accurate determination of the respective proton tensor, preferentially in single crystals, and an advanced theoretical treatment (DFT) of the complex.

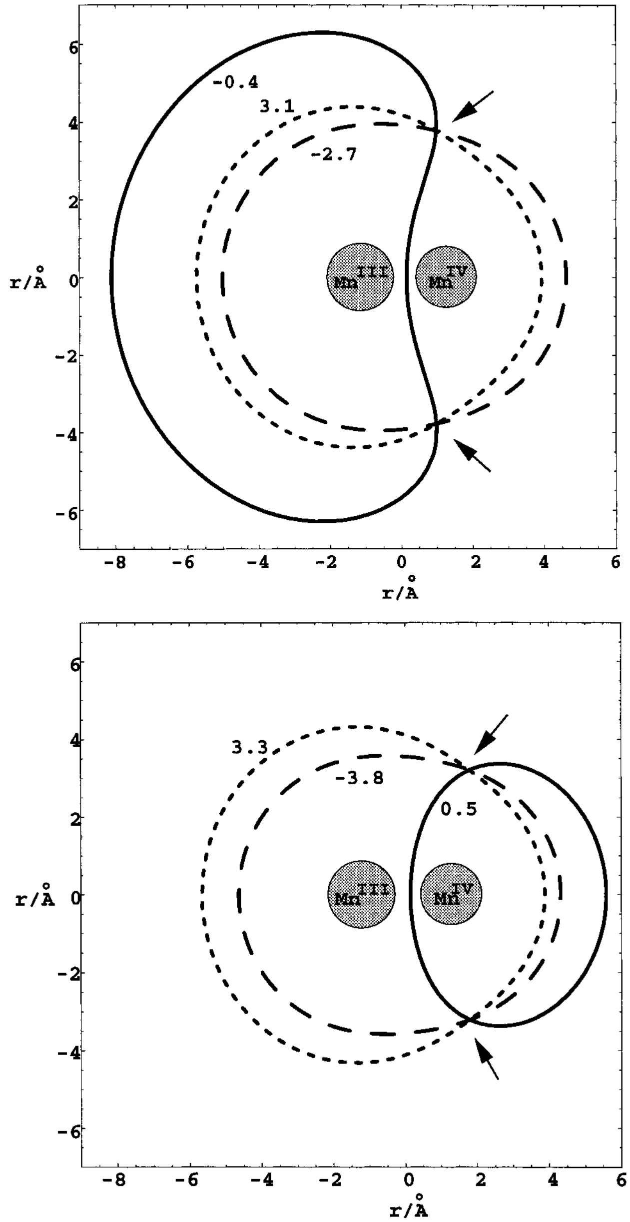

Figure 9. Representation of three lines corresponding to constant values of dipolar hf tensor components $A'_x = -0.4$ MHz, $A'_y = -2.7$ MHz, and $A'_z = 3.1$ MHz (top) and $A'_x = 0.5$ MHz, $A'_y = -3.8$ MHz, and $A'_z = 3.3$ MHz (bottom). The Mn−Mn distance was set to 2.56 Å, as found in **1**. A hypothetical proton with a dipolar hf tensor $\mathbf{A}' = (-0.4, -2.7, 3.1)$ MHz (top) and $\mathbf{A}' = (0.5, -3.8, 3.3)$ MHz (bottom) would then be located at the intersection of the three lines; these are indicated by arrows. Since a rotation of the proton about the line joining the Mn ions does not alter the tensor, the proton can be located on the resulting circle.

Protons bound to N2, N3, N5, and N6 are present only in **1** and **4**. Within experimental error, we found their hf tensors to be identical in both complexes. The isotropic part of the tensor on the Mn^{III} side is twice as large as that of the corresponding tensor on the Mn^{IV} side and has opposite sign. Protons at N1 and N4 are unique to complex **4**; in **1** and **2**, the CH_2CH_2 fragment that connects the tacn rings is attached to these nitrogens. The dipolar part of the hfc is more rhombic than that for the protons bound to the equatorially nitrogen. At N1 and N4, the protons are located almost perpendicular to the line connecting the Mn ions, where the tensor would be perfectly axial ($\Theta = 0$).

In the tacn ligands, there are two possible orientations for protons connected to the same carbon: one is pointing away from the metal and the other toward the manganese (e.g., positions C1a and C1b). On the Mn^{III} side, these two orientations can be distinguished. Since the overall hyperfine coupling is smaller on the Mn^{IV} side, here a distinction is not possible. The hf tensors in the tacn macrocycle are very similar within experimental error in complexes **1**, **2**, and **4** (Table 3). This is strong evidence that the geometry of the tacn ligand is conserved within all these complexes. A difference is expected to occur when the tacn macrocycles are additionally connected by the CH_2CH_2 fragment. Experimentally, we observe only a minor change in one tensor component (from 5.3 to 5.6 MHz). A difference is seen for the tensors within the CH_2CH_2 fragment in complexes **1** and **2** and the tensors in the bridging OAc group. They are located between the Mn ions. This is a region where small geometrical changes have a large effect on the magnitude of the tensors, according to the extended point-dipole model.

Assignments in complexes **5** and **6** were based largely on structural similarities and on this point-dipole model (Table 4). Isotropic hfc's were not found for protons in these complexes.

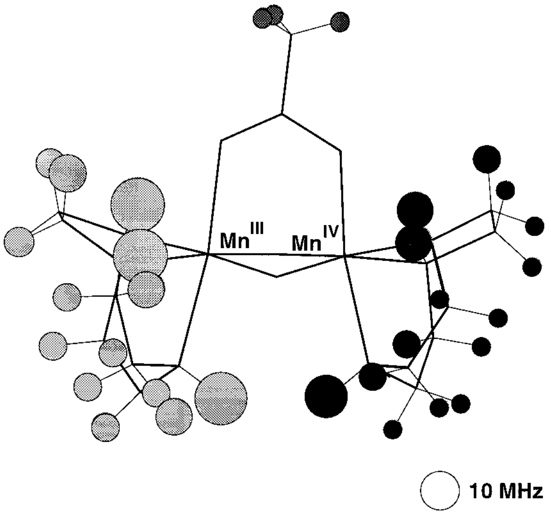

Figure 10. Model complex **4** with assigned hfc's obtained from experimental data. The area of the circles is proportional to the absolute value of the largest measured proton hf tensor component. Most of the tensors are purely dipolar. Note that this is not a spin-density distribution for which the circles would be proportional to A_{iso}. The hfc's on the Mn^{III} side are larger than those on the Mn^{IV} side. This is indicated by different shadings (for details, see Table 3).

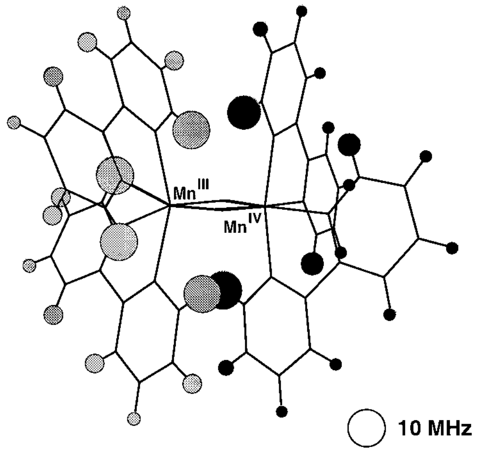

Figure 11. Model complex **5** with assigned hfc's obtained from experimental data. The area of the circles is proportional to the largest proton hf tensor component (Table 4) (for further details, see Figure 10).

Table 5. Experimentally Observed ^{14}N hfc's and Quadrupole Couplings (MHz) from ^{14}N ENDOR

complex	$\lvert A\rvert$	$\lvert e^2qQ\rvert/h$	reference
1	9.8	2.20	this work
2	9.4	2.24	this work
4	9.6	2.20	this work
5	9.5	2.9	this work
6	9.7	3.0	this work
CYCLAM[a]	9.23	2.98	32
TMPA[b]	11.20	3.02	32
5	9.4	2.9	33

[a] CYCLAM: $Mn^{III}Mn^{IV}(\mu\text{-oxo})_2$-bis-1,4,8,11-tetraazacyclotetradecane. [b] TMPA: $Mn^{III}Mn^{IV}(\mu\text{-oxo})_2$-bis-(tris-2-methylpyridyl)amine.

Most of the tensors were axial, with the exception of the protons close to the region between the Mn ions. Tensors for the protons attached to positions in which the ligands are different in **5** and **6** (e.g., C17, C27) are small, because of the large distance to the Mn ions.

Because some calculated dipolar tensor components are very similar, we had to assign the same experimentally observed tensor component to different protons in several cases. An example shall be given to explain the difficulty: in the tacn macrocycles, protons on the Mn^{III} side have almost axial hf tensors. If we draw a contour plot for such an axial tensor similar to those given in Figure 9, we do not obtain definite crosspoints, but the three lines are almost identical (on the Mn^{III} side). This means that there is a large uncertainty regarding the molecular position for this tensor, or in other words, many proton positions within the molecule lead to only slightly different hf tensors, which then result in a superposition of resonances and in broadened ENDOR lines.

Figures 10 and 11 clearly show that the hyperfine couplings are larger on the Mn^{III} side by a factor of about 2, as predicted by the vector coupling model. A special case is presented by the methyl protons in the bridging acetato fragment. They are located in the region between the manganese ions. However, here the influence of Mn^{III} is expected to dominate that of Mn^{IV}. Proton hf tensors in this region show a rather large deviation from axiality. The same situation is met with the protons in the CH_2CH_2 fragment that connects the tacn ligands in **1** and **2**.

Apart from the fact that we had to assign several tensor components to more than one proton position, we derived a consistent assignment for all hf tensors to proton positions in our complexes (see Tables 3 and 4).

3.8. ^{14}N cw-ENDOR. In Figure 7, several lines in the low-frequency ENDOR range of complex **1** could be assigned unambiguously to ^{14}N nuclei. According to the ENDOR resonance condition for nuclei with $I = 1$, two line pairs appear centered around $A_{^{14}N}/2 = 4.9$ MHz (**1**), split by the quadrupole coupling $^3/_2P_i = 3.3$ MHz and by twice the Larmor frequency $2\nu_{^{14}N} \approx 2$ MHz (see eq 11). The respective lines are indicated by arrows in Figure 7. This pattern was found for all studied complexes and led to the identification of one strongly coupled ^{14}N nucleus with the hf and quadrupole components given in Table 5. The additional lines in this frequency range show that there is coupling to further ^{14}N nuclei which could, however, not be evaluated with confidence.

Two types of ^{14}N hyperfine couplings have been observed in exchange-coupled nitrogen-ligated $Mn^{III}Mn^{IV}$ complexes:[32,33] a larger one in the frequency range around 10 MHz and a smaller one below 5 MHz. If the excess spin density resides in the d_{z^2} orbital of Mn^{III},[32] the larger coupling would arise from Fermi contact interaction between this orbital and the nitrogen 2s orbitals, i.e., nitrogen bound axially to Mn^{III}. This hfc can be observed by ENDOR but is not detectable by ESEEM, since the "cancellation" condition is not met. We assign the larger ^{14}N hfc observed in our ENDOR spectra to the ^{14}N bound in axial position to Mn^{III}. Our values agree well with data obtained earlier[32,33] (see Table 5).

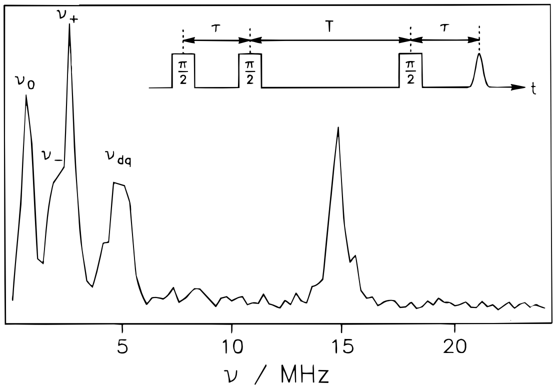

Figure 12. Three-pulse (stimulated echo) 2D-ESEEM spectrum of model complex **4** after Fourier transformation in the T domain and light projection along the τ axis. Experimental data: 512 × 128 points; ν_{MW}, 9.7687 GHz; field, 347.6 mT; $\pi/2$, 16 ns; τ_o, 120 ns; $\Delta\tau$, 16 ns; T_o, 120 ns; ΔT, 16 ns; *T*, 4.2 K. Top: Pulse sequence used in the experiment.

In all measured complexes, the values of A_z are similar, showing that the nitogen coordination is the same. It is interesting that also the related quadrupole couplings are the same within experimental error for the tacn-type ligation in **1**, **2**, and **4** (nitrogen, sp^3 hybridization). For the bpy- and phen-ligated complexes **5** and **6**, the e^2qQ/h is different, as indicated by the different electronic structure of the nitrogen nuclei in these ligands (nitrogen, sp^2 hybridization). In cyclam and tmpa,[32] the quadrupole coupling was found to be similar to that in bpy and phen, indicating a similar electric field gradient. The smaller quadrupole coupling in **1**, **2**, and **4** compared with that in **5** and **6** results most probably from the increased local charge symmetry in the former complexes.

3.9. ^{14}N-ESEEM. To resolve smaller ^{14}N hfc's below 5 MHz, ESEEM spectroscopy was used. Favorable experimental conditions could be found only for complex **4**. For **1** and **2**, significantly shorter T_1 times prevented the detection of similar spectra for these complexes so far. Complex **5** has been previously investigated by Britt[82] and Ivancich et al.[21] Therefore, **5** and the similar complex **6** were not studied here.

Figure 12 shows the light projection of a complete three-pulse 2D-ESEEM experiment performed on complex **4**. The spectrum directly yields the zero-field nuclear quadrupole transitions ν_-, ν_0, and ν_+ (see eqs 13−15) of one ^{14}N nucleus, from which the nuclear quadrupole coupling e^2qQ/h and the asymmetry parameter η are directly obtained. Furthermore, a "double-quantum" transition ν_{dq} is observed (eq 16), yielding the effective hyperfine coupling ($A_{eff} = 2.9$ MHz). The data are collected in Table 6. A strong line from the proton nuclei with some shoulders is seen near the Larmor frequency which has not been further evaluated. The spectrum and data are similar to those reported for **5**[82] and also to those reported for methylated Mn-catalase by Ivancich et al.[21] (see Table 6). The authors attribute the shape of the spectrum to the fact that the observed nitrogen hfc is too large, so the cancellation condition is not met. In our case, $\nu_{^{14}N} = 1.05$ MHz and $A_{eff}/2 = 1.45$ MHz. These parameters satisfy the cancellation condition $|\nu_n - |A|/2| < 2K/3$.

---

(82) Britt, R. D. Electron Spin Echo Spectroscopy in Photosynthesis. Ph.D. thesis, University of California, Berkeley, 1988.

Table 6. Experimentally Observed ^{14}N hfc's and Quadrupole Couplings (MHz) from ESEEM

complex	$\|A_{eff}\|$	$\|e^2qQ\|/h$	η	reference
4	2.9	2.5	0.6	this work
5	2.8	2.3		82
Mn-catalase	2.3	2.44		85
Mn-catalase	2.45	2.34	0.51	21

Due to the limited spectral resolution in our spectrum, the ν_- and ν_+ peaks are not very well separated, but in contrast to the work by Ivancich et al.,[21] they can still be distinguished. From the intensity of the peaks in our spectrum, we conclude that these are not intermodulation peaks. A final point in favor of our interpretation is the fact that lines corresponding to our measured A_{eff} and e^2qQ/h could be found in the ^{14}N ENDOR spectrum of **4**, although they were not yet evaluated in the ENDOR experiments.

The small hfc can be assigned either to the equatorially bound nitrogens on the Mn^{III} side or to the nitrogens on the Mn^{IV} side. If it were assigned to the Mn^{IV} side, we would expect from the vector coupling model a hfc that is twice as large on the Mn^{III} side (5−7 MHz). Since we were not able to observe such a coupling, we conclude that this small hfc originates from the equatorial nitrogens bound to Mn^{III}. This assignment is supported by an estimate made by Tan et al.[32] These authors calculated a hfc of $A_{eff} \approx 3$ MHz for nitrogens bound equatorially to Mn^{III}. The hfc of the respective nitrogens on the Mn^{IV} side is then expected to be (−)2 MHz.[32]

4. Summary and Conclusion

In this work, we have studied several exchange-coupled dinuclear manganese complexes using EPR techniques. The complexes could be divided into two classes: one containing two μ-oxo bridges, and the other containing two μ-oxo and a μ-OAc bridge. The latter three complexes were increasingly sterically hindered by joining the two tacn ligands and by exchange of NH groups with NCH_3 groups. For all complexes, EPR spectra were recorded at two frequency bands. Simulations of X- and Q-band EPR spectra yielded precise **G** and ^{55}Mn hf tensor data for each complex. Tacn-type ligated complexes showed distinct rhombic tensors. The isotropic parts of the tensors were smaller than those of the bpy-type complexes. Insight into the generation of rhombicity of the **G** and hf tensors and information about the orientation of **G** and ^{55}Mn hf tensor axes in the complexes could be obtained by use of a vector coupling model that incorporates structural parameters into the calculation of the tensors for the combined system. This is an important prerequisite for further magnetic resonance studies of these and related systems *in vivo* and *in vitro*, e.g., for orientation-selection ENDOR experiments and for the analysis of the electronic structure in general.

The magnetic interaction of the electron spin with ligand nuclear spins was examined using electron nuclear double-resonance (ENDOR) experiments. By the combined use of differently structured compounds, H/D exchange, and orientation selection, specific proton positions within the molecules could be assigned to various hf tensors. Hyperfine interaction basically results from dipolar coupling in the complexes, with the exception of protons that are directly bound to the first ligand sphere (nitrogen). For these protons, a significant isotropic coupling is obtained. To calculate the dipolar hyperfine interactions, we developed an extended point-dipole model which yielded values for all proton hf tensors in the complexes. Comparison of measured hf splittings with calculated ones identified all hfc's that led finally to a complete and consistent assignment of proton positions to experimental hf tensors.

This work has shown that the extended point-dipole model can be used with confidence to identify dipolar hfc's in exchange-coupled systems containing a dinuclear metal core. The approach that we used to assign experimental hfc's can now be employed in further studies to identify and assign hfc's. Randall et al.[36] and Willems et al.[61] recently used this approach to deduce proton positions from measured hf tensors.

ENDOR experiments in the nitrogen frequency range identified a large ^{14}N coupling assigned to ligand nitrogens that are directly bound to Mn. These, most probably, have an appreciable isotopic hfc. This hfc could be assigned to the nitrogens axially bound to Mn^{III}. Further ^{14}N lines in the ENDOR spectra that result from smaller couplings could not be evaluated with confidence. By use of ESEEM spectroscopy, however, we found a small ^{14}N hfc in **4** and assigned this coupling to the equatorially bound nitrogens on the Mn^{III} side. The information available on two ^{14}N hfc's can be used to compare the systems to each other and, moreover, to *in vivo* systems such as manganese catalase. The data can further be used to provide evidence for direct ligation of nitrogens in metalloenzymes.[32] ^{14}N nuclear quadrupole parameters are, for example, smaller in complexes **5** and **6** as compared with those of pyridine-type bases,[83] which indicates a decrease of the electric field gradient upon binding to the metal. A similar ligation leads to nuclear quadrupole parameters similar to those found for tacn and dtne, whereas different parameters were obtained for different types of ligation, e.g., tacn and bpy. Thus, these parameters can provide a sensitive tool for ligand identification and yield information about the local electronic structure via the electric field gradient.

More insight into the orientation of tensor axes with respect to the molecular structure can be obtained from single crystals of the model complexes. This is, however, difficult since interactions between the electron spins of neighboring complexes in the lattice make the EPR analysis of single crystals difficult. Here one could employ diamagnetically dilute single crystals. By this approach, the exact orientation of all tensor axes could be determined.

The analysis of the **G** and hyperfine tensor axes that we proposed in this paper would benefit if there were more accurate intrinsic data for Mn^{3+} and Mn^{4+} ions in different environments. The accuracy of the **G** tensor measurements can be improved by applying higher magnetic fields, e.g., by performing experiments at W-band (94 GHz) frequencies. Furthermore, at these frequencies, orientation selection is faciliated in powder ENDOR experiments because of a better separation of the **G** tensor components.[84] Work along these lines is in progress in our laboratory.[68,69]

Acknowledgment. This paper is dedicated to Prof. M. P. Klein and Prof. K. Sauer (UC Berkeley), in recognition of their pioneering work in the field of oxygenic photosynthesis. We thank Dr. H. Käss for his help with the ESEEM measurements. Financial support from the Deutsche Forschungsgemeinschaft (Lu 315/14-1) and Fonds der Chemischen Industrie (to K.W. and W.L.) is gratefully acknowledged.

Appendix

One way to find the principal values for the **G** tensor of the effective spin is to keep one **g** tensor fixed and transform the

---

(83) Lucken, E. A. C. *Nuclear Quadrupole Coupling Constants*; Academic Press: New York, 1989.

(84) Rohrer, M.; MacMillan, F.; Prisner, T. F.; Gardiner, A. T.; Möbius, K.; Lubitz, W. *J. Phys. Chem. B* **1998**, *102*, 4648.

(85) Dikanov, D. J.; Tsvetkov, V. S. K.; Goldfeld, M. G. *Dokl. Biophys. (Engl. Transl.)* **1988**, *302*, 107.

other **g** tensor to this reference system. A convenient reference for the common system is Mn$^{\mathrm{III}}$, since $\mathbf{g}_{\mathbf{III}}$ is axial, with the unique axis being the *z*-axis. The transformation is then given by

$$\mathbf{G}' = 2\mathbf{g}'_{\mathbf{III}} - \mathbf{T}\mathbf{g}_{\mathrm{IV}}\mathbf{T}^{\mathrm{T}} \qquad (21)$$

where the primed and the unprimed tensors relate to the common and the individual coordinate systems, respectively ($\mathbf{g}'_{\mathbf{III}} = \mathbf{g}_{\mathbf{III}}$). The other two tensor axes are the molecular *x*- and *y*-axes. With the assumption of coincident *y*-axes, the G'^{y} component can be calculated immediately by

$$G'^{y} = 2g^{y}_{\mathrm{III}} - g^{y}_{\mathrm{IV}} \qquad (22)$$

The remaining transformation is a rotation about the *y*-axis:

$$\begin{pmatrix} G'^{zz} & G'^{zx} \\ G'^{xz} & G'^{xx} \end{pmatrix} = 2\begin{pmatrix} g^{z}_{\mathrm{III}} & \\ & g^{x}_{\mathrm{III}} \end{pmatrix} - \begin{pmatrix} \cos\alpha & \sin\alpha \\ -\sin\alpha & \cos\alpha \end{pmatrix}\begin{pmatrix} g^{z}_{\mathrm{IV}} & \\ & g^{x}_{\mathrm{IV}} \end{pmatrix}\begin{pmatrix} \cos\alpha & -\sin\alpha \\ \sin\alpha & \cos\alpha \end{pmatrix} \qquad (23)$$

The combined **G** tensor then has to be diagonalized to obtain the principal values, since the rotation creates off-diagonal matrix elements. The principal values G'^{x} and G'^{z} are

$$G'^{x/z} = {}^{1}\!/_{2}[(2\Sigma_1 - \Sigma_2) \pm \sqrt{4\Delta_1{}^{2} - 4\Delta_1\Delta_2\Delta_\Theta + \Delta_2{}^{2}}]$$

with

$$\Sigma_1 = (g^{z}_{\mathrm{III}} + g^{x}_{\mathrm{III}}) \qquad \Sigma_2 = (g^{z}_{\mathrm{IV}} + g^{x}_{\mathrm{IV}})$$

$$\Delta_1 = (g^{z}_{\mathrm{III}} - g^{x}_{\mathrm{III}}) \qquad \Delta_2 = (g^{z}_{\mathrm{IV}} - g^{x}_{\mathrm{IV}})$$

$$\Delta_\Theta = \cos^2\alpha - \sin^2\alpha$$

Supporting Information Available: Tables of crystal data and structure refinement, atomic coordinates, bond lengths and angles, anisotropic displacement parameters, and hydrogen coordinates for complexes **1**, **2**, and **3** a view of the crystal structures of complexes **1** and **2** (26 pages, print/PDF). See any current masthead page for ordering information and Web access instructions.

JA9827548